Highly eccentric inspirals into a black hole

Thomas Osburn, Niels Warburton, and Charles R. Evans

Phys. Rev. D **93**, 064024 — Published 9 March 2016

DOI: 10.1103/PhysRevD.93.064024

Highly eccentric inspirals into a black hole

Thomas Osburn,[1] Niels Warburton,[2] and Charles R. Evans[1]
[1]*Department of Physics and Astronomy, University of North Carolina, Chapel Hill, North Carolina 27599, USA*
[2]*MIT Kavli Institute for Astrophysics and Space Research,*
Massachusetts Institute of Technology, Cambridge, MA 02139, USA

We model the inspiral of a compact stellar-mass object into a massive non-rotating black hole including all dissipative and conservative first-order-in-the-mass-ratio effects on the orbital motion. The techniques we develop allow inspirals with initial eccentricities as high as $e \sim 0.8$ and initial separations as large as $p \sim 50$ to be evolved through many thousands of orbits up to the onset of the plunge into the black hole. The inspiral is computed using an osculating elements scheme driven by a hybridized self-force model, which combines Lorenz-gauge self-force results with highly accurate flux data from a Regge-Wheeler-Zerilli code. The high accuracy of our hybrid self-force model allows the orbital phase of the inspirals to be tracked to within ~ 0.1 radians or better. The difference between self-force models and inspirals computed in the radiative approximation is quantified.

PACS numbers: 04.25.dg, 04.30.-w, 04.25.Nx, 04.30.Db

I. INTRODUCTION

Relativistic compact binary systems are promising astrophysical sources of gravitational waves. Detection of gravitational waves by ground-based detectors, such as LIGO [1], VIRGO [2] or KAGRA [3], or future space-based detectors, such as eLISA [4], will be facilitated by accurate theoretical waveform templates. These theoretical templates will also allow the parameters of the source to be determined, which will inform population studies of compact objects as well as allow precision tests of general relativity in the strong-field regime. Producing suitable waveform templates requires solving the two body problem in a general relativistic context which, unlike its Newtonian counterpart, does not have a closed form solution. A number of different techniques exist to approximate solutions to this problem, each applicable to a different class of system depending upon the orbital separation or the mass-ratio of the two bodies.

When the two bodies are widely separated, the post-Newtonian expansion can be employed [5]. This expansion performs well in the slow adiabatic phase of the inspiral but becomes less accurate as the orbital separation decreases. Once the strong-field regime is entered, for comparable-mass systems, no analytic approximations can be made and the full non-linear Einstein equations must be numerically solved on a supercomputer [6, 7]. More extreme-mass-ratio systems are beyond the current reach of numerical relativity due to the high resolution requirements around the smaller body and the wide separation of time scales in the problem. In this regime one turns to black hole perturbation theory [8–10]. In addition to the above approaches there is also effective-one-body theory [11–13], which incorporates elements from all three of the aforementioned schemes.

In this work we are interested in the inspiral of a stellar-mass compact object (such as a black hole, neutron star, or white dwarf) into a substantially more massive black hole. When the binary system consists of a supermassive black hole of mass $M \sim 10^5$–$10^7\, M_\odot$ and a smaller compact object of mass $\mu \sim 1$–$10\, M_\odot$ (so the mass ratio $\epsilon = 10^{-5}$–10^{-7}) the emitted gravitational waves will be in the frequency band detectable by space-based detectors such as eLISA. Such extreme-mass-ratio-inspirals (EMRIs) are expected to provide clean tests of general relativity in the strong-field regime [14–17] (unspoiled by environmental effects [18]). Less extreme mass-ratio binary systems are also of interest as they will be observable with Advanced LIGO [16, 19]. For this to occur, intermediate mass black holes must exist with masses $M \sim 10^2$–$10^4 M_\odot$ [20]. A binary system consisting of an intermediate mass black hole and a smaller compact object of mass $\mu \sim 1$–$10\, M_\odot$ is called an intermediate mass-ratio inspiral (IMRI).

Modeling EMRIs and IMRIs is achieved by perturbatively expanding the Einstein field equations in powers of the (small) mass ratio. Typically, the smaller body is modeled as a point particle and the particle's interaction with its metric perturbation gives rise (after regularization) to a self-force that drives the inspiral [21–26]. Calculating this self-force has been a major research effort for the past 15 years that has met with great success, both in computing the gravitational self-force [27–32] and conservative gauge-invariant quantities [33–36], which have been compared with results from other approaches to the two-body problem [37–48].

For computing inspirals it is important to calculate the self-force to high accuracy because in order to detect and accurately extract source parameters from an E/IMRI waveform the phase evolution will need to be tracked to within ~ 0.1 radians or less. This requirement is challenging because from the time an EMRI enters eLISA's passband to when the binary's components merge there is an orbital phase accumulation of order $\epsilon^{-1} \sim 10^5$–10^7 radians. A second challenge is the need to calculate the self-force for highly eccentric orbits, as we expect astrophysical sources to enter the eLISA passband with eccentricities peaked around $e \sim 0.7 - 0.8$ [49].

To meet our accuracy goal it is necessary to go beyond leading-order flux balance evolutions (so-called radiative or secular approximations) [50, 51] and include conservative and subleading-order dissipative corrections to the orbital motion. This we achieve by using a recently developed frequency-domain Lorenz-gauge self-force code [52]. However, the raw output of that code is still not sufficient to reach our accuracy goal across the entire parameter space of inspirals (especially at high eccentricity). Instead, as argued in [52], the Lorenz-gauge results can be augmented with high-accuracy flux data from a Regge-Wheeler-Zerilli (RWZ) code to produce a hybrid self-force scheme. This paper shows that hybridization in action and confirms that our accuracy requirements can be met. Importantly, by accurately reaching eccentricities as high as $e \sim 0.8$, the hybrid code breaks a barrier where traditionally it was thought that frequency-domain codes [30, 53] must give way to time-domain calculations.

We compute our inspirals by calculating the Lorenz-gauge self-force for over 9500 geodesics of a Schwarzschild black hole. The hybrid self-force is constructed by combining the Lorenz-gauge data with RWZ flux results from over 40,000 geodesics. The resulting forces are interpolated across the orbital parameter space. We then evolve our orbits using an osculating element scheme. It is key to point out that by using the *geodesic self-force* we are making an approximation. The true self-force is a functional of the past history of the *inspiraling motion*, whereas in our scheme (and other recent ones [54, 55]) we take the self-force at each instance to be that of a particle that has moved along a background geodesic for all time. These two self-forces are thought to differ at the first post-adiabatic order [56], and there is ongoing work to quantify the error that is induced in the inspiral phase when using this approximation [57–59]. As mentioned, the same approach was taken in Ref. [54].

This project is distinguished, however, in several respects. Our inspirals meet observationally motivated accuracy goals in contrast with Ref. [54]. These accuracy goals are achieved through a novel interpolation scheme, a more dense basis of self-force models, parameterization of the orbit in a way that accounts for the separatrix, and, as mentioned, a hybridized self-force. We are able to cover the full astrophysical range of eccentricities and separations rather than the low-eccentricity/small-separation or quasi-circular evolutions modeled by Refs. [54] and [55], respectively. We also introduce a new technique based on Pade approximants to mitigate a well-known ill-conditioning problem met when calculating the Lorenz gauge self-force [30, 52]. Finally, we quantify the phase discrepancy between self-force models and inspirals computed in the radiative approximation.

The layout of this paper is as follows. In Sec. II we review how the self-force influences an inspiral and in Sec. III we discuss our approach to computing inspirals using the osculating element scheme detailed in Sec. IV. In Secs. V and VI we present our hybridized self-force model and its interpolation over the parameter space of geodesics. In Sec. VII we discuss how to compare inspirals computed using the full self-force with inspirals computed using an approximate self-force. Our main results are then presented in Sec. VIII and we conclude with some final remarks in Sec. IX. Throughout this paper we set $c = G = 1$, use metric signature $(-+++)$ and the sign conventions of Misner, Thorne, and Wheeler [60].

II. EFFECTS OF THE SELF-FORCE ON AN INSPIRAL

The smaller body's interaction with its own metric perturbation gives rise to a self-force that causes the motion to deviate from a geodesic of the background spacetime of the larger black hole. In practice we calculate this self-force perturbatively, expanding the Einstein field equations in powers of the mass ratio, $\epsilon = \mu/M \ll 1$. How we compute the self-force from a suitably regularized metric perturbation will be discussed in Sec. V. The self-force drives the motion off of a background geodesic[1] in the following way

$$\mu u^\beta \nabla_\beta u^\alpha = F^\alpha_{(1)} + F^\alpha_{(2)} + \mathcal{O}(\epsilon^4), \tag{2.1}$$

where u^α is the body's four-velocity and ∇ denotes the covariant derivative with respect to the background metric. By $F^\alpha_{(n)}$ we denote the n^{th}-order self-force, i.e., the part proportional to the $n+1$ power of the mass ratio. Alternatively, we may use the covariant form of (2.1) for the evolution of u_α, which requires the covariant form of the self-force F_α. This latter form of the equation of motion, it turns out, plays an important role in our hybrid method, as described in Sec. V.

In the geodesic self-force approximation we can in addition split the force, at each order, into a conservative part, F^α_{cons}, attributed to the time-symmetric part of the gravitational field and a dissipative part, F^α_{diss}, due to the time-antisymmetric part of the gravitational field

$$F^\alpha = F^\alpha_{\text{diss}} + F^\alpha_{\text{cons}}. \tag{2.2}$$

The dissipative part is responsible for radiation reaction effects such as the decay of orbital energy and angular momentum. The conservative part perturbs the orbital parameters, but does not cause a secular decay of the orbit. See Fig. 1 for an illustration of these effects.

The dissipative self-force can be further split into two parts: an adiabatic part $F^{\alpha(\text{diss})}_{\text{ad}}$, whose components vary slowly over an inspiral on the radiation reaction timescale and represents some average over the orbital timescale, and an oscillating part $F^{\alpha(\text{diss})}_{\text{osc}}$, whose components oscillate on the orbital timescale. We can thus write for the

---

[1] Alternatively, the motion can be considered as a geodesic in a regular effective space-time [9, 24]. Here we use the "forced motion in the background spacetime" picture but both viewpoints are equally valid.

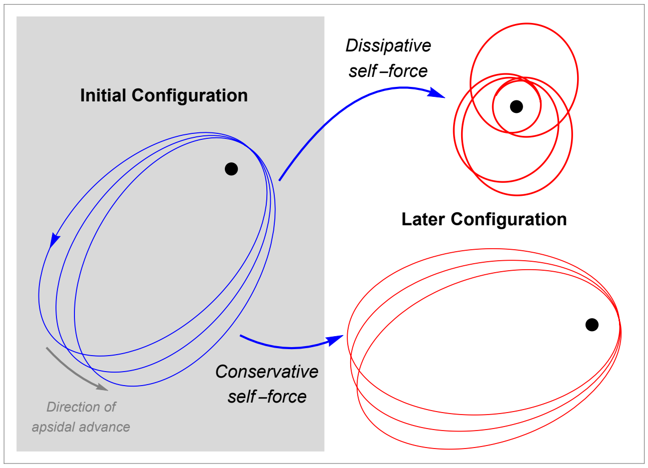

FIG. 1. Illustration of dissipative and conservative self-force influences on the inspiral. On the left, the motion of the compact body around the central black hole is taken to be counter-clockwise, as is then the apsidal advance of the orbit. On the right top, the dissipative self-force is responsible for the secular decay of energy and angular momentum, which causes the orbit to shrink and shed eccentricity. In contrast (right bottom), the conservative self-force does not affect the long-term average of the orbital constants. Instead it is responsible for a slower than usual apsidal advance [61] and tiny periodic changes in the shape of the eccentric orbit. Both effects occur simultaneously during a physical inspiral.

full self-force

$$F^\alpha = F^{\alpha(\text{diss})}_{\text{ad}} + F^\alpha_{\text{osc}}, \tag{2.3}$$

$$F^\alpha_{\text{osc}} \equiv F^{\alpha(\text{diss})}_{\text{osc}} + F^{\alpha(\text{cons})}. \tag{2.4}$$

Unfortunately, the adiabatic/oscillatory split is ambiguous at this point. The general intent is to take

$$F^{\alpha(\text{diss})}_{\text{ad}} \equiv \langle F^{\alpha(\text{diss})} \rangle, \tag{2.5}$$

$$F^{\alpha(\text{diss})}_{\text{osc}} = F^{\alpha(\text{diss})} - \langle F^{\alpha(\text{diss})} \rangle, \tag{2.6}$$

but to be precise this requires a specific definition for the average $\langle \ \ \rangle$ over the orbital timescale. The ambiguity comes because the averaging can be performed with respect to different curve parameters and, again because of the orbital eccentricity, there is a difference in averaging contravariant versus covariant components. See the discussion by Pound and Poisson in [62] on this ambiguity and its effect on defining an “adiabatic,” “secular,” or “radiative” approximation. In this paper, even though we avoid making the adiabatic approximation, we nonetheless have a use for this decomposition in defining our hybrid scheme, and single out a particular definition for the averaging process. This specific choice is discussed further below and in Sec. V.

Assuming that some definition is adopted, at any moment in time the adiabatic and oscillatory parts will be comparable in size. However, if we compute the oscillatory part along a bound geodesic of the background spacetime (i.e., compute the self-force but do not actually apply it), the average over one orbit of $F^{\alpha(\text{diss})}_{\text{osc}}$ vanishes by construction (this is true also of $F^{\alpha(\text{cons})}$). If instead the self-force is applied and the orbit allowed to evolve, then $F^{\alpha(\text{diss})}_{\text{osc}}$ (and $F^{\alpha(\text{cons})}$) will nearly average to zero over one radial orbital period, with the residual being of order $\mathcal{O}(\epsilon)$ relative to a typical instantaneous magnitude.

The smallness of this average implies a gradual, adiabatic inspiral, and is a needed justification for using the geodesic self-force. A number of authors have considered how these different parts of the self-force influence the inspiral phase [63–65] with one of the most rigorous discussions given by Hinderer and Flanagan [66]. We review several key results and highlight where previous work has employed the various components of the self-force in computing inspirals.

With an E/IMRI there is a large accumulation of orbital phase from the point when the binary enters, say, the eLISA passband until merger. The leading-order part to the orbital phase enters at $\mathcal{O}(\epsilon^{-1})$ and is driven by the abovementioned adiabatic, first-order-in-the-mass-ratio, dissipative self-force $F^{\alpha(\text{diss})}_{(1)\text{ad}}$. Conveniently, this component of the self-force can be related to the orbit-averaged asymptotic fluxes[2], which sidesteps the need for a more complicated, local calculation of the self-force from the metric perturbation at the particle. A number of authors have used this approach to calculate the leading-order phase evolution of generic inspirals into Kerr black holes [50, 51], though at the cost of missing some effects available within the first order perturbation.

In a regular perturbation calculation, the next effects in the cumulative phase would be at $\mathcal{O}(\epsilon^0)$. However, it is known that for generic inspirals in Kerr spacetime, certain resonant configurations will occur that contribute to the cumulative orbital phase at $\mathcal{O}(\epsilon^{-1/2})$. These transient resonances take place when the radial and polar orbital frequencies are in a low-integer ratio [70] and will generically occur a few times during any inspiral [71]. Resonant orbits are an active area of research [72–74] but will not be considered further in this work as we concentrate on inspirals in Schwarzschild spacetime.

The next contributions to the orbital phase lie at $\mathcal{O}(\epsilon^0)$. These include the conservative part of the first-order self-force, the oscillatory part of the dissipative first-order self-force, and the adiabatic part of the dissipative second-order self-force. (At this order, there is also expected to be a difference between using the geodesic self-force instead of the true self-force.) The first two contributions require a local calculation of the self-force and in recent years there has been great progress evaluating these quantities [27–30, 32, 52]. The first low-eccentricity

---

[2] Flux balance arguments allow the evolution of the orbital energy and angular momentum to be computed. For generic orbits in Kerr spacetime the evolution of the Carter constant is computed using methods introduced by Mino [67–69]

inspirals in Schwarzschild spacetime computed incorporating these two components were presented in Ref. [54]. The evolution of quasi-circular inspirals has also been explored [55]. As yet there have been no calculations of the second-order-in-the-mass-ratio self-force but the appropriate formalism and calculation techniques are emerging [75–80].

To summarize, the influence of each component of the self-force on the phase of the waveform in the inspiral, as measured, for example, by using the cumulative radial phase Φ_r as a proxy, is

$$\Phi_r = \underbrace{\kappa_0\,\epsilon^{-1}}_{\text{adiabatic: } F^{\alpha(\text{diss})}_{(1)\text{ad}}} + \underbrace{\kappa_{1/2}\,\epsilon^{-1/2}}_{\text{resonances (Kerr only)}} + \underbrace{\kappa_1\,\epsilon^{0}}_{\substack{\text{post-1-adiabatic:}\\ F^{\alpha(\text{cons})}_{(1)} + F^{\alpha(\text{diss})}_{(1)\text{osc}} + F^{\alpha(\text{diss})}_{(2)\text{ad}}}} + \cdots, \tag{2.7}$$

where the κ coefficients are dimensionless, of order unity, and depend on the ingress and egress (or merger) frequencies in a particular detector, but not on the mass ratio ϵ. The adiabatic dissipative part of the self-force comes in at lower order than the remaining parts of the self-force, and accordingly must be computed with greater accuracy in order to affect the phase error at the same level. Even though our present calculations account for all first-order-in-the-mass-ratio contributions in the geodesic self-force, we purposefully make the split into adiabatic dissipative and oscillatory dissipative parts so that these two pieces can be computed, in the hybrid scheme, to their separate fractional accuracies.

III. OVERVIEW OF OUR APPROACH

Formally, the self-force is a functional of the entire past history of the inspiral. Letting $z^\alpha(\tau)$ denote the particle's inspiraling worldline, with τ being proper time, we can write the self-force as $F^\alpha(\tau) \equiv F^\alpha[z^\alpha(\tau' < \tau)]$. In order to compute an inspiral in a self-consistent manner one must solve for the worldline using Eq. (2.1) whilst simultaneously computing the perturbation in the gravitational field and its effects in generating the local self-force.

To date, such a self-consistent inspiral has only been computed for the case of a scalar particle [81]. Instabilities with the time-domain evolution of the low l-modes of the Lorenz-gauge self-force currently stand in the way of computing self-consistent inspirals in the gravitational case (see Ref. [31] for a discussion of these gauge instabilities). This provides part of the motivation for using the geodesic self-force approach to computing the inspiral. A secondary motivation comes from noting the high computational cost of evolving inspirals in the time-domain. Currently available technology (for the case of a scalar particle) allows for the computation of inspirals with a few tens of periastron passages at the cost of weeks of runtime on hundreds of CPU cores [82]. Certainly, in the near future, such time-domain approaches will not be extensible to computing the many hundreds of thousands of periastron passages that occur in an astrophysical EMRI. Furthermore, it will be required to compute many thousands of inspirals in order to construct a suitably dense template bank of waveforms for use in matched filtering searches. In the method we employ here, a single preprocessing step takes a few thousand CPU hours and once that is complete each inspiral can be computed in a matter of minutes.

The geodesic self-force approach stems from the key observation that, as an EMRI evolves adiabatically, the inspiral is closely approximated at each moment by a background geodesic that is tangent to the true (inspiralling) worldline. At each moment the true self-force is approximated by the (geodesic) self-force that would exist if the motion were not driven off the background geodesic. Differences between the true inspiral and the background geodesic are greatest in the distant past, and the tail integral that gives rise to the local self-force is expected to have falling contributions for $\tau' \ll \tau$. Similar higher-order effects due to differences between true evolution and fixed-orbit calculations occur in post-Newtonian theory [83]. In this picture, inspirals are evolved by replacing F^α in Eq. (2.1) with $F^\alpha_G(\tau) \equiv F^\alpha[z^\alpha(\tau); z^\alpha_G(\tau')]$ where $z^\alpha_G(\tau')$ is the worldline of the background geodesic tangent to $z(\tau)$. Working with the geodesic self-force has a key advantage that during the inspiral phase the tangent geodesic is bound and strictly periodic. The periodic nature of the tangent geodesic allows for an efficient frequency-domain calculation of the self-force [30, 52]. Moreover, working in the frequency-domain avoids the gauge instabilities observed in time-domain evolutions. Although frequency-domain codes can compute self-force data rapidly, they are not sufficiently quick to allow direct on-the-fly inspiral evolutions. Instead we interpolate the self-force data over the applicable range of the orbital parameter space. A new and efficient interpolation procedure is presented in Sec. VI.

Previous applications of geodesic self-force evolution [54, 55] only probed small eccentricities ($e \lesssim 0.2$). As astrophysical EMRIs are expected to have high eccentricities [49], we have worked to expand the range of the technique to model eccentricities up to $e \lesssim 0.8$. Furthermore, a self-force model must be sufficiently accurate to capture correctly the phase evolution of the inspiral for matched-filtering purposes. As the previous section noted in Eq. (2.7), we do not need to know all pieces of the self-force to the same accuracy. (This is fortunate since some parts of the self-force are more challenging to compute than others.) This motivates the hybrid self-force method discussed in [52]. As summarized in Table I, the most sensitive part of the self-force–the adiabatic dissipative part–can be calculated from fluxes obtained with a very accurate RWZ code, while the oscillatory part of the dissipative self-force and the conservative part can be computed with a Lorenz gauge code [52]. The separate

TABLE I. The required accuracies for an archetypal EMRI system with a massive black hole of mass $10^6 M_\odot$ orbited by a stellar mass black hole of mass $10 M_\odot$ ($\epsilon = 10^{-5}$). The scaling of the phase evolution from Eq. (2.7) implies the accuracy with which we need to obtain the self-force. Row two of the table shows the precision in the self-force required to track the phase evolution to within ~ 0.1 radians. Row three gives the codes we use to compute the various components, and row four shows the precision in the output data from these codes. The wide range in precision of the Lorenz-gauge code is a function of the orbital eccentricity. At present there are no codes able to compute the second-order self-force in the strong-field (though Ref. [84] uses a PN flux formula to explore the effects of the second-order self-force upon an quasi-circular evolution).

	$F^{\alpha(\mathrm{diss})}_{(1)\mathrm{ad}}$	$F^{\alpha}_{(1)\mathrm{osc}}$	$F^{\alpha(\mathrm{diss})}_{(2)\mathrm{ad}}$
Required Accuracy	10^{-7}	10^{-2}	10^{-2}
Code	RWZ [85, 86]	Lorenz [52]	$\cdots$
Code Accuracy	10^{-10}-10^{-9}	10^{-7}-10^{-3}	$\cdots$

required accuracies are listed in Table I. How data from the two codes are combined is discussed in Sec. V B.

Finally, we must address how the geodesic self-force approximation will influence the phasing of the modeled orbit. As mentioned above, arguments have been made that the error will enter at $\mathcal{O}(\epsilon^0)$ (see Sec. 1.5.6 of Ref. [56]). This might seem discouraging as the geodesic self-force approximation is introducing an error in the phase at the same order as the oscillatory conservative and dissipative effects we have worked hard to include. The only way to assess how problematic this is to our approach is to compare our evolution with a fully self-consistent one. As mentioned, this is not yet possible for the gravitational case. Work is ongoing, however, to make this comparison for scalar self-force evolutions. Preliminary work comparing the self-consistent time-domain code of Ref. [81] and a geodesic scalar self-force inspiral code constructed using the techniques of Ref. [53] indicates that, although the phase error might enter at $\mathcal{O}(\epsilon^0)$, the coefficient must be small (in fact so small it has yet to be measured despite concerted effort [57–59]).

IV. OSCULATING ELEMENT DESCRIPTION OF MOTION

Our approach is to solve Eq. (2.1) using the geodesic self-force as the forcing term. Similar to Newtonian celestial mechanics calculations, we recast the equation of motion into one for the evolution of osculating elements of the inspiral. The resulting inspiral can be immediately interpreted in a geometric manner and the numerical output from the self-force codes can be more easily linked to the long-term evolution code.

In the osculating element approach the true (accelerated) worldline, $z(\tau)$, is taken to be tangent to a background geodesic worldline $z_G(\tau)$ at each time τ. As the true worldline advances, the parameters of the background geodesic smoothly evolve. At each instance the tangent (or "osculating") geodesic is characterized [62] by a set of orbital elements I^A, with the true worldline represented by a continuous sequence of elements $I^A(\tau)$. With the four-velocity of the tangent geodesic given by $u^\alpha_G(I^A,\tau) = \partial_\tau z^\alpha_G(I^A,\tau)$, we can write

$$z^\alpha(\tau) = z^\alpha_G(I^A,\tau), \qquad u^\alpha(\tau) = u^\alpha_G(I^A,\tau). \tag{4.1}$$

We thus seek equations of motion for the set of osculating elements. This procedure was first outlined by Pound and Poisson [62] for motion about a Schwarzschild black hole. Extension of the idea to motion in Kerr spacetime was given by Gair et al. [87]. The resulting equations of motion take the form

$$\frac{\partial z^\alpha_G}{\partial I^A}\frac{\partial I^A}{\partial \tau} = 0, \qquad \mu \frac{\partial u^\alpha_G}{\partial I^A}\frac{\partial I^A}{\partial \tau} = F^\alpha. \tag{4.2}$$

Our explicit choices for I^A for bound motion and the resulting equations of motion are given in the next subsection. It is important to note that the osculating element approach is simply a recasting of Eq. (2.1) and is valid for any forcing term[3]; no small forcing approximation is made.

A. Bound geodesics in Schwarzschild spacetime

We consider in this paper bound and eccentric motion around a Schwarzschild black hole. Schwarzschild coordinates $x^\alpha = (t, r, \theta, \varphi)$ are adopted, in which the line element takes the standard form

$$ds^2 = -f\,dt^2 + f^{-1}dr^2 + r^2\left(d\theta^2 + \sin^2\theta\,d\varphi^2\right), \tag{4.3}$$

where $f(r) = 1 - 2M/r$. The geodesic worldline is given by a set of functions $z^\alpha_G(\tau) = [t_p(\tau), r_p(\tau), \theta_p(\tau), \varphi_p(\tau)]$, parameterized by (for example) proper time τ. Without loss of generality the motion is confined to the equatorial plane, $\theta = \pi/2$. The geodesic four-velocity u^α_G is given by

$$u^\alpha_G = \left(\frac{\mathcal{E}}{f_p}, u^r_G, 0, \frac{\mathcal{L}}{r_p^2}\right), \tag{4.4}$$

where $f_p \equiv f(r_p)$ and $\mathcal{E}$ and $\mathcal{L}$ are the specific energy and angular momentum, respectively. The constraint $u^\alpha_G u^G_\alpha = -1$ yields an expression for u^r_G:

$$(u^r_G)^2 = \mathcal{E}^2 - f_p\left(1 + \frac{\mathcal{L}^2}{r_p^2}\right). \tag{4.5}$$

---

[3] so long as the tangent geodesic remains bounded

We parameterize the geodesic with the eccentricity, e, and semi-latus rectum, p, which are related to the radial turning points $r_{\min}$ and $r_{\max}$ via

$$p = \frac{2r_{\max}r_{\min}}{M(r_{\max}+r_{\min})}, \qquad e = \frac{r_{\max}-r_{\min}}{r_{\max}+r_{\min}}. \tag{4.6}$$

Eq. (4.6) and the roots of Eq. (4.5) give the relationship between (p,e) and ($\mathcal{E}$,$\mathcal{L}$):

$$\mathcal{E} = \sqrt{\frac{(p-2)^2-4e^2}{p(p-3-e^2)}}, \qquad \mathcal{L} = \frac{pM}{\sqrt{p-3-e^2}}. \tag{4.7}$$

Orbits are bound when $e < 1$ and are stable when $p > 6 + 2e$.

In self-force calculations it is convenient to reparameterize the orbital motion (i.e., all the curve functions) with the relativistic anomaly χ [88], defined so that

$$r_p(\chi) = \frac{pM}{1+e\cos\left[\chi-\chi_0\right]}. \tag{4.8}$$

The parameter χ_0 specifies the value of χ at pericentric passage.

Eq. (4.8) can be used with Eqs. (4.4) and (4.7) to derive the following initial value equations for the development of the orbit

$$\frac{d\tau_p}{d\chi} = \frac{Mp^{3/2}}{(1+e\cos v)^2}\sqrt{\frac{p-3-e^2}{p-6-2e\cos v}}, \tag{4.9}$$

$$\frac{dt_p}{d\chi} = \frac{r^2}{M(p-2-2e\cos v)}\sqrt{\frac{(p-2)^2-4e^2}{p-6-2e\cos v}}, \tag{4.10}$$

$$\frac{d\varphi_p}{d\chi} = \sqrt{\frac{p}{p-6-2e\cos v}}, \tag{4.11}$$

where $v \equiv \chi - \chi_0$. Without loss of generality we can choose initial conditions $\varphi_p|_{\chi=0} = 0$, $t_p|_{\chi=0} = 0$, $\tau_p|_{\chi=0} = 0$, in which case changes in χ_0 serve, for example, to alter the orientation of the orbit.

The periods of one radial libration measured in t and τ are denoted by T_r and $\mathcal{T}_r$, respectively. They are given by

$$T_r = \int_0^{2\pi}\frac{dt_p}{d\chi}d\chi, \qquad \mathcal{T}_r = \int_0^{2\pi}\frac{d\tau_p}{d\chi}d\chi. \tag{4.12}$$

The amount of azimuthal angle accumulated in one radial period, T_r, is given by

$$\Delta\varphi = \int_0^{2\pi}\frac{d\varphi_p}{d\chi}d\chi. \tag{4.13}$$

Each orbit has associated with it two fundamental frequencies. One is a libration-type frequency associated with the radial motion and the other is a rotation-type frequency associated with the average rate at which the orbital azimuthal angle accumulates. These two frequencies are defined via

$$\Omega_r \equiv \frac{2\pi}{T_r}, \qquad \Omega_\varphi \equiv \frac{\Delta\varphi}{T_r}. \tag{4.14}$$

B. Evolution of orbital elements

For the osculating element scheme, the set of orbital elements we evolve are

$$I^A = (p, e, \chi_0, t_p, \varphi_p). \tag{4.15}$$

The elements (p, e) are "principal elements" that describe the spatial shape of the tangent geodesic but not its orientation. The orientation of the orbit is set by the "positional element" χ_0. The last two elements (t_p, φ_p) track the evolution of the time and angular coordinate of the orbit.

The evolution of I^A follows from Eqs. (4.2), (4.9), (4.10), and (4.11). We also use the orthogonality of the self-force and the four-velocity, $F^\alpha u_\alpha = 0$, to manipulate how the components of F^α appear in the equations. The following is our formulation of the evolution equations for e, p, and χ_0

$$\frac{de}{d\chi} = \frac{a_{(t)}(e,p,v)F^t + a_{(\varphi)}(e,p,v)F^\varphi}{\mu\, q(e,p,v)}, \tag{4.16}$$

$$\frac{dp}{d\chi} = \frac{b_{(t)}(e,p,v)F^t + b_{(\varphi)}(e,p,v)F^\varphi}{\mu\, q(e,p,v)}, \tag{4.17}$$

$$\frac{d\chi_0}{d\chi} = \frac{c_{(r)}(e,p,v)F^r + c_{(\varphi)}(e,p,v)F^\varphi}{\mu\, q(e,p,v)}, \tag{4.18}$$

$$a_{(t)} \equiv Mp(p-3-e^2)(6+2e^2-p)(1+e\cos v)^2 \times (2-p+2e\cos v)\sqrt{(p-2)^2-4e^2}, \tag{4.19}$$

$$a_{(\varphi)} \equiv M^2p^{5/2}(1-e^2)(3+e^2-p) \times \left[4e^2+(p-6)(p-2)\right], \tag{4.20}$$

$$b_{(t)} \equiv 2M\,e\,p^2(3+e^2-p)(p-2-2e\cos v) \times (1+e\cos v)^2\sqrt{(p-2)^2-4e^2}, \tag{4.21}$$

$$b_{(\varphi)} \equiv 2M^2e\,p^{7/2}(p-4)^2(p-3-e^2), \tag{4.22}$$

$$c_{(r)} \equiv Mp^2(3+e^2-p)(2e+(p-6)\cos v) \times (1+e\cos v)^2\sqrt{p-6-2e\cos v}, \tag{4.23}$$

$$c_{(\varphi)} \equiv M^2p^{5/2}\sin v(3+e^2-p)\Big(2(p-6)(3-p) + e\cos v\left[(4e^2-(p-6)^2)+2e(p-6)\cos v\right]\Big), \tag{4.24}$$

$$q \equiv e(p-6-2e)(p-6+2e) \times (1+e\cos v)^4\sqrt{p-6-2e\cos v}. \tag{4.25}$$

The equations for t_p and φ_p are unchanged from Eqs. (4.10) and (4.11). See Ref. [62] for the detailed derivation of an equivalent set of evolution equations for the osculating elements.

Specifying the initial values of the elements I^A is equivalent to specifying the initial position and velocity on Eq. (2.1). For motion in a plane there are three initial positions and two initial velocities (three minus the one for the normalization condition $u^\alpha_G u^G_\alpha = -1$), which matches the number of initial values we specify for I^A.

For a long-term evolution, all of the differential equations (4.16), (4.17), (4.18), (4.10), and (4.11) are integrated simultaneously (along with (4.9) if desired), while continually updating the self-force components as derived from the instantaneous background geodesic.

V. CALCULATION OF THE LORENZ GAUGE SELF-FORCE WITH A HYBRID SCHEME

Recent frequency-domain codes are now able to rapidly compute the self-force in Lorenz gauge along a geodesic orbit [30, 52]. In this work we use the code presented in Ref. [52] but with an improvement to the source integration method described in Ref. [86]. Unfortunately, for some high eccentricity inspirals that interest us here, that code is still not sufficiently accurate to reach the accuracy requirements laid out in Table I. However, the amount by which each part of the self-force influences the inspiral phasing suggests a solution: use a highly accurate RWZ code to compute gauge-invariant fluxes and then use that data to obtain the leading-order (orbit-averaged) contribution, $F^{\alpha\text{diss}}_{(1)\text{ad}}$, of the self-force. The remaining parts of the first-order self-force are then supplied by the Lorenz-gauge code. This "hybrid self-force" approach was sketched out in Sec. V.B of Ref. [52]. We give further details below in Sec. V B. First, however, we briefly outline the Lorenz-gauge self-force and describe an added improvement that has been made to the Lorenz-gauge code that helped increase its range of applicability and reduced its runtime.

A. Lorenz-gauge self-force

The finite mass of the small body induces a perturbation over the background metric $g_{\mu\nu}$. Working to first-order-in-the-mass-ratio, we may write the full spacetime metric as $\mathrm{g}_{\mu\nu} = g_{\mu\nu} + h_{\mu\nu}$, with metric perturbation (MP) $h_{\mu\nu}$. Defining the trace-reversed MP by $\bar{h}_{\mu\nu} \equiv h_{\mu\nu} - \frac{1}{2} g_{\mu\nu} h$ (with $h = h_{\alpha\beta}\, g^{\alpha\beta}$), the Lorenz-gauge condition is given by

$$\nabla_\nu \bar{h}^{\mu\nu} = 0, \tag{5.1}$$

where ∇ is compatible with the background metric. The Lorenz-gauge linearized Einstein equations for the first-order-in-the-mass-ratio MP is then given by

$$\Box \bar{h}_{\mu\nu} + 2R^{\alpha}{}_{\mu}{}^{\beta}{}_{\nu}\, \bar{h}_{\alpha\beta} = -16\pi T_{\mu\nu}, \tag{5.2}$$

where $\Box \equiv g^{\alpha\beta}\nabla_\alpha\nabla_\beta$, $R^{\alpha}{}_{\mu\beta\nu}$ is the Riemann tensor in the background and $T_{\mu\nu}$ is the stress-energy tensor. The last is taken to be that of a point-mass moving along a fixed, bound geodesic of the background spacetime.

The spherical symmetry of the background Schwarzschild spacetime and the periodicity of the source allow for a tensor spherical-harmonic and Fourier decomposition of Eq. (5.2) that fully decouples the individual tensor-harmonic and Fourier modes (though for each mode the metric perturbation amplitudes generally remain coupled). The field equations for each mode are reduced to a coupled set of ordinary differential equations (ODEs), which we solve numerically with suitable boundary conditions to construct the retarded solution. Within this procedure each mode of the retarded MP is finite at the particle's location, but the sum over modes diverges there. We employ the method of extended homogeneous solutions to ensure the Fourier sum converges exponentially [89] and construct the self-force using the mode-sum regularization scheme of Barack and Ori [23]. We also employ additional regularization parameters from Ref. [90] that speed up the convergence of the mode-sum. Full details of the code we use are given in Refs. [52, 86].

One challenge with the frequency-domain Lorenz gauge method arises when constructing the inhomogeneous solutions from a suitable basis of homogeneous solutions using the standard variation of parameters approach. In this approach, a Wronskian matrix of homogenenous solutions is assembled, which must be inverted. This matrix becomes ill-conditioned when the mode frequency $\omega = m\,\Omega_\varphi + n\,\Omega_r$ is small, where m and n are integers [30]. Arbitrarily small frequencies are encountered in the neighborhood of orbital resonances where the ratio Ω_φ/Ω_r is a rational number. Without any algorithm to alleviate this issue the smallest-frequency modes that can be computed with machine precision are typically around $|\omega M| \gtrsim 10^{-3}$. Akcay et al. employed novel techniques to handle frequencies as small as $|\omega M| \gtrsim 10^{-4}$ [30]. Even with this improved limit, large fractions of orbital parameter space remain excluded from accurate calculation. Osburn et al. [52] used quad-precision numerical integration and other novel techniques to handle frequencies as low as $|\omega M| \gtrsim 10^{-6}$ [52]. Unfortunately, that improvement comes at considerable added computational expense.

As an alternative, we developed a new method to calculate asymptotic boundary conditions that utilizes the diagonal Pade approximant (DPA). With this change, we are able to handle frequencies as small as $|\omega M| \gtrsim 10^{-5}$ while avoiding use of quad-precision numerical integration. We outline the method here as it is applied in the odd-parity sector, though the same techniques carry over to the even-parity sector. To begin, as shown in [52] it is straightforward to ensure that the condition number of the Wronskian matrix is unity at the start of each numerical integration for homogeneous modes by using a QR-preconditioning technique. The key to then limiting the growth of the condition number during numerical integration is to begin the integrations as close to the source region as possible, while maintaining required accuracy in the initial conditions.

In the odd-parity sector, for a given multipole and frequency mode, the field equations involve two coupled fields. We can represent the homogeneous solutions with a vector $\tilde{\boldsymbol{\mathcal{B}}}$. Asymptotically, as $r \to \infty$, the retarded radial fields have a dependence on $e^{i\omega r_*}$, where r_* is the usual tortoise coordinate defined by $dr_*/dr = f^{-1}$. In order to place boundary conditions for our numerical scheme at a finite radius, r_{out}, we usually make an asymptotic expansion of the fields of the form

$$\tilde{\boldsymbol{\mathcal{B}}}_j^{\text{Asym}}(r_{\text{out}}) = e^{i\omega r_{*\text{out}}} \sum_{s=0}^{s_{\max}} \begin{bmatrix} \alpha^{(0)}_{j,s} \\ \alpha^{(1)}_{j,s} \end{bmatrix} \rho^s_{\text{out}}, \tag{5.3}$$

$$\rho_{\text{out}} \equiv (\omega r_{\text{out}})^{-1}, \tag{5.4}$$

where $j = 0, 1$ and $r_{*\text{out}} \equiv r_*(r_{\text{out}})$. This asymptotic expansion has limited use unless evaluated in the wave-zone $r_{\text{out}} \gg |\omega|^{-1}$. At low frequencies, a long numerical integration is required to reach the source region. As an alternative to this standard approach, we attempted use of an expansion based on the DPA

$$\tilde{\boldsymbol{\mathcal{B}}}_j^{\text{DPA}}(r_{\text{out}}) = e^{i\omega r_{*\text{out}}} \begin{bmatrix} A^{(0)}_j(r_{\text{out}}) \\ A^{(1)}_j(r_{\text{out}}) \end{bmatrix} \tag{5.5}$$

$$A^{(i)}_j(r_{\text{out}}) \equiv \frac{\displaystyle\sum_{s=0}^{s_{\max}/2} \beta^{(i)}_{j,s}\, \rho^s_{\text{out}}}{\displaystyle 1 + \sum_{s=1}^{s_{\max}/2} \gamma^{(i)}_{j,s}\, \rho^s_{\text{out}}} \tag{5.6}$$

where $s_{\max}$ is assumed to be even. It is straightforward to compute the DPA coefficients $\beta^{(i)}_{j,s}$ and $\gamma^{(i)}_{j,s}$ from the asymptotic expansion coefficients $\alpha^{(i)}_{j,s}$ (see for example Ref. [91]). Quad-precision arithmetic is used to compute the DPA coefficients because the linear systems that describe them become increasingly ill-conditioned when $s_{\max}$ is taken to be large. This minor use of quad-precision in setting boundary conditions is of minimal computational cost compared to the previous use of quad-precision in the ODE integrations described in Ref. [52]. The benefit of the DPA is that the boundary conditions can be set at an r_{out} that is much closer to the source region, thus allowing rapid machine-precision numerical integration of the ODEs.

There is no a priori guarantee that the DPA will be an improvement over the standard asymptotic expansion, but we have tested its validity numerically. One appropriate numerical test for how well $\tilde{\boldsymbol{\mathcal{B}}}_j^{\text{DPA}}$ or $\tilde{\boldsymbol{\mathcal{B}}}_j^{\text{Asym}}$ satisfies Eq. (5.2) at a given r is to use the relevant expansion as initial conditions, perform a numerical integration of distance $\Delta r \sim |\omega^{-1}|$, and compare the result to the expansion re-evaluated at $r + \Delta r$. We show in Fig. 2 that the DPA allows initial conditions to be given at approximately a factor of 10 closer to the source region than the standard asymptotic expansion. The decreased integration distance and reduced rise of condition number allow frequencies as small as $|\omega M| \geq 10^{-5}$ to be included, which we found sufficient for an accurate exploration of the astrophysically-relevant portion of orbital parameter space.

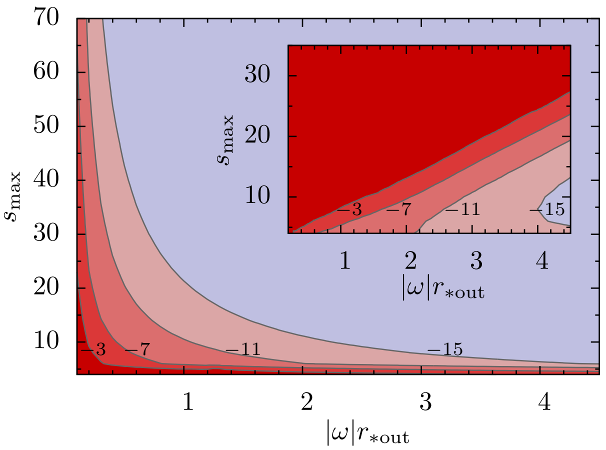

FIG. 2. The effectiveness of the diagonal Pade approximant (DPA) method for constructing boundary conditions to the homogeneous Lorenz-gauge field equations compared to the standard asymptotic expansion. We calculated the relative error for each basis of homogeneous solutions with both methods and the worst case is reported. The contours are of constant relative error with $\log_{10}$ scaling, and are given as a function of the number of expansion terms $s_{\max}$ and the location of $r_{*\text{out}}$. The larger plot shows the relative error of the DPA while the inset shows the relative error of the asymptotic expansion. It is apparent that the DPA allows initial conditions to be given at approximately a factor of 10 closer to the source region than the asymptotic expansion. This reduces the computation time and improves accuracy by limiting the growth of the condition number. Here we consider the odd-parity case of $(l, \omega) = (2, 10^{-4}M^{-1})$. Similar results are observed for the even-parity sector.

B. Hybrid self-force

Ideally the Lorenz-gauge self-force code would be used to precompute forces that would drive the inspiral via the osculating element method presented in Sec. IV. Unfortunately, and despite best efforts, at high eccentricities the present numerical implementation in the Lorenz-gauge code fails to attain the required accuracy in all parts of self-force, as outlined in Table I. The drop in accuracy for orbits with $e \gtrsim 0.5$ stems from the need to compute and sum over many tens of thousands of Fourier-harmonic modes.

Fortunately, it is not necessary to know all parts of the self-force with equal accuracy (again see Table I). The most critical accuracy requirement is on the adiabatic, orbit-averaged part of the dissipative self-force. This part of the self-force can be determined from energy and angular momentum fluxes at infinity and the horizon, and does not require a local calculation. We can obtain the fluxes from the Lorenz-gauge code or from a separate RWZ code. This is the basis of the hybrid scheme outlined previously in [52], which augments the Lorenz-gauge results with highly accurate flux data from a RWZ code. In this section we review how to construct such a "hybrid self-force," which is sufficiently accurate to compute inspirals with phase error less than 0.1 radians.

It begins by noting that for a background geodesic $u_t = -\mathcal{E}$ and $u_\varphi = \mathcal{L}$ are constants of the motion, and thus the covariant form of Eq. (2.1) for the t and φ components will determine gradual changes in the particle's specific energy and angular momentum. Multiplying by μ we get rates of change with respect to proper time of the particle's energy and angular momentum. Integrating these over proper time to find averages, the orbit-averaged rate of gain (or loss) of energy and angular momentum with respect to coordinate time due to the self-force is

$$\mu\langle\dot{\mathcal{E}}\rangle = -\frac{1}{T_r}\int_0^{\mathcal{T}_r} F_t \, d\tau = -\frac{\mathcal{T}_r}{T_r}\langle F_t\rangle_\tau, \tag{5.7}$$

$$\mu\langle\dot{\mathcal{L}}\rangle = \frac{1}{T_r}\int_0^{\mathcal{T}_r} F_\varphi \, d\tau = \frac{\mathcal{T}_r}{T_r}\langle F_\varphi\rangle_\tau. \tag{5.8}$$

In these expressions the overdot indicates differentiation with respect to coordinate time, t, angle brackets with a τ subscript indicate a proper-time average, and angle brackets with no subscript indicate a coordinate time average. The rate at which the particle loses energy and angular momentum must be balanced by the averaged asymptotic fluxes. This balance gives

$$\mu\langle\dot{\mathcal{E}}\rangle = -\langle\dot{E}\rangle, \qquad \mu\langle\dot{\mathcal{L}}\rangle = -\langle\dot{L}\rangle, \tag{5.9}$$

where $\langle\dot{E}\rangle$ and $\langle\dot{L}\rangle$ are the average rates at which energy and angular momentum are radiated, respectively. These balance formulas can then be related to the adiabatic self-force components via

$$F_t^{\text{ad}} = \langle F_t\rangle_\tau = \frac{T_r}{\mathcal{T}_r}\langle\dot{E}\rangle, \qquad F_\varphi^{\text{ad}} = \langle F_\varphi\rangle_\tau = -\frac{T_r}{\mathcal{T}_r}\langle\dot{L}\rangle. \tag{5.10}$$

Harking back to our discussion in Sec. II, the hybrid method settles on adopting the average over proper time to define the adiabatic part of the self-force.

The object then is to remove $F^{\text{ad}}_{t/\varphi}$ from our Lorenz-gauge self-force and replace it with the values computed at much higher accuracy with our RWZ code. We can separate out the adiabatic component of the self-force from our numerical Lorenz-gauge results by noting that the oscillatory part of the self-force averages to zero over an orbital period. This motives a Fourier decomposition of the self-force in proper time,

$$F_\alpha = \tilde{a}_0^{(\alpha)} + \sum_{n=1}^{\infty}\left[\tilde{a}_n^{(\alpha)}\cos(2\pi n\tau/\mathcal{T}_r) + \tilde{b}_n^{(\alpha)}\sin(2\pi n\tau/\mathcal{T}_r)\right], \tag{5.11}$$

where $\alpha = \{t, \varphi\}$ (we address the radial component of the self-force momentarily). Comparing to Eq. (2.3) we see that

$$F_\alpha^{\text{ad}} = \tilde{a}_0^{(\alpha)} \tag{5.12}$$

$$F_\alpha^{\text{osc}} = \sum_{n=1}^{\infty}\left[\tilde{a}_n^{(\alpha)}\cos(2\pi n\tau/\mathcal{T}_r) + \tilde{b}_n^{(\alpha)}\sin(2\pi n\tau/\mathcal{T}_r)\right]. \tag{5.13}$$

The ingredients are now at hand and we construct the hybrid self-force via

$$F_\alpha^{\text{hyb}}(p,e,v) = F_\alpha^{\text{ad(RWZ)}}(p,e) + F_\alpha^{\text{osc(Lor)}}(p,e,v), \tag{5.14}$$

with explicit dependence on orbital parameters indicated.

In computing $F_\alpha^{\text{ad(RWZ)}}$ we use a RWZ code based off of Refs. [85, 86]. In constructing $F_\alpha^{\text{osc(Lor)}}$ we make use of the discrete Fourier transform (DFT) to compute the amplitudes in Eq. (5.11) (see Ref. [86] where these techniques are used in a similar application). The algorithmic roadmap for constructing F_α^{hyb} for a given (p,e) is then the following:

1. *Compute Lorenz gauge self-force:* See subsection V A. Our code is configured to return the contravariant components of the self-force F^α at a large number of time samples equally spaced in v. We construct the covariant self-force at the same v samples by lowering the index using the background metric.

2. *Interpolate $F_\alpha(v)$ using DFT:* Compute the coefficients $\tilde{g}_n^{(\alpha)}$ and $\tilde{h}_n^{(\alpha)}$ of the Fourier series expansion

$$F_\alpha = \sum_{n=0}^{N}\left[\tilde{g}_n^{(\alpha)}\cos(nv) + \tilde{h}_n^{(\alpha)}\sin(nv)\right] \tag{5.15}$$

   using a DFT applied to the equally-spaced-in-v numerical data. Eq. (5.15) can then be used to construct $F_\alpha(v)$ at arbitrary values of v.

3. *Compute list of v values consistent with equal τ spacing:* Special functions [92] or root finding of the Fourier representation of $\tau(v)$ [86] can be used to choose a list of equally spaced τ values and find the corresponding list of v values. We use the root finding method.

4. *Compute τ-Fourier series of F_α:* Construct the equally-spaced-in-τ values of F_α using the v values from the previous step and interpolating using Eq. (5.15). The DFT of this data gives the desired Fourier amplitudes $\tilde{a}_n^{(t/\varphi)}$ and $\tilde{b}_n^{(t/\varphi)}$ in Eq. (5.11). A strong check is to compare $\tilde{a}_0^{(t)}$ with $\langle\dot{E}\rangle^{\text{RWZ}}T_r/\mathcal{T}_r$ and $\tilde{a}_0^{(\varphi)}$ with $-\langle\dot{L}\rangle^{\text{RWZ}}T_r/\mathcal{T}_r$. These should agree to as many digits as are attainable from the Lorenz gauge results (see, for example, Table V of Ref. [52]).

5. *Construct hybrid force:* The hybrid force is constructed using Eq. (5.14). The adiabatic piece is computed with the RWZ fluxes using Eq. (5.10). The oscillatory part is computed using the Fourier coefficients from the previous step with Eq. (5.12).

6. *Construct contravariant hybrid force with equal v spacing:* Our osculating elements scheme is formulated with the contravariant components, therefore we raise the index with the background metric. Note that this causes F^α_{ad} to vary over an orbit. In the section that follows, we interpolate over the (p, e) parameter space and find it convenient to resample with equal v spacing.

So far we have ignored hybridization of the r component of the self-force. In principle F^r_{hyb} could be constructed from the orthogonality condition $F^\alpha_{\text{hyb}} u_\alpha = 0$. Instead of doing so, we express the e and p evolution equations in terms of only F^t_{hyb} and F^φ_{hyb}, eliminating need of the r component of the self-force in those two equations. There remains the equation for χ_0 evolution. Rewriting that equation in terms of the t and φ components of the self-force is not numerically practical as it introduces a division by u^r which is zero at the orbital turning points. Fortunately, in the χ_0 evolution the conservative part of the self-force dominates over the dissipative part by a factor of ϵ (see Sec. VIII A and Fig. 8). Since hybridization only (subtly) alters the dissipative part, hybridization would affect the evolution of χ_0 at a level many orders of magnitude below the dominant behavior.

VI. INTERPOLATION OF THE HYBRID SELF-FORCE ACROSS THE (p, e) PARAMETER SPACE

In order to numerically integrate the osculating element equations (4.16)-(4.18) we need to supply the self-force at arbitrary values of (p, e, v). Whilst our Lorenz-gauge code is capable of rapidly computing the self-force, it is not sufficiently quick to allow it to be directly coupled to the integration of the osculating elements. Instead we populate the relevant portion of the (p, e) parameter space with a few thousand data points and interpolate to the intervening values. This section describes our interpolation procedure.

A. Sampling the hybrid self-force

Equally sampling the hybrid self-force in (p, e) space is not optimal, especially near the separatrix where small changes in p can lead to large changes in the value of the self-force. The behaviour of the radiated fluxes near the separatrix [93] suggests that a good parameterization in this region is $y(x) \sim -1/\ln x$, where $x \equiv p-2e-6$. However, this choice is not well suited to points away from the separatrix so we construct a function that smoothly transitions $y(x)$ to be proportional to x away from the separatrix

$$y(x) \equiv \begin{cases} (x+8)w(x,6) - \dfrac{35[1-w(x,6)]}{\ln{(x/80)}}, & x < 6 \\ x+8, \quad x \geq 6 \end{cases}, \tag{6.1}$$

where $w(x, d)$ is a smooth transition function of width d given by

$$w(x,d) \equiv \frac{1}{2} + \frac{1}{2}\tanh\left[\tan\left(\frac{\pi x}{2d}\right) - \cot\left(\frac{\pi x}{2d}\right)\right]. \tag{6.2}$$

We computed the adiabatic part of the self-force using the RWZ gauge code on a grid with $\Delta y = 0.1$, $y_{\text{min}} = 4$, $y_{\text{max}} = 59$, $\Delta e = 0.01$, $e_{\text{min}} = 0.01$, and $e_{\text{max}} = 0.83$. We computed the oscillatory part of the self-force (and the full self-force F^α) using the Lorenz gauge code on a grid with $\Delta y = 0.2$, $y_{\text{min}} = 4.4$, $y_{\text{max}} = 59$, $\Delta e = 0.02$, $e_{\text{min}} = 0.02$, and $e_{\text{max}} = 0.82$ (see Fig. 3). There are some gaps in the data, especially in the oscillatory part where we avoid orbits with non-zero frequencies ω_{mn} smaller than $10^{-5}M^{-1}$.

For the adiabatic self-force we computed data for 43875 unique orbits at a cost of 2054 CPU hours. For the oscillatory, Lorenz-gauge self-force we computed data for 9602 unique orbits at a cost of 2308 CPU hours. We also explored spacing the data using a reduced order model [94]. Our initial tests suggested this would be a promising method to reduce the computational burden but we did not pursue if further. Such methods might be important though when interpolating the self-force over the larger parameter space of geodesics in Kerr spacetime.

B. Interpolation of the self-force

The periodicity of the geodesic self-force suggests using a Fourier series for interpolation in time [54]

$$F^\alpha = \mu^2 \sum_{n=0}^{n_{\text{max}}} \left[a^\alpha_n(e,y)\cos(nv) + b^\alpha_n(e,y)\sin(nv)\right]. \tag{6.3}$$

The Fourier coefficients $a^\alpha_n(e, y)$ and $b^\alpha_n(e, y)$ can then be interpolated across orbital parameter space (e and y). We truncate the Fourier series at $n_{\text{max}} = 13$ because we have found that to be a sufficient number of harmonics to represent the force at our accuracy goals. Our self-force codes output the Fourier amplitudes a^α_n and b^α_n directly by computing the DFT of data with a large number of equally spaced v samples. Note that for the adiabatic part $b^\alpha_n = 0$. As an example we will consider the interpolation of a^α_n, but the same techniques apply to b^α_n. We separately interpolate the Fourier amplitudes of the adiabatic, oscillatory, and non-hybrid parts of the self-force.

A similar method was used by Ref. [54] to interpolate the (non-hybrid) self-force. In that work they interpolated over a parameter space spanning $6 + 2e < p < 12$

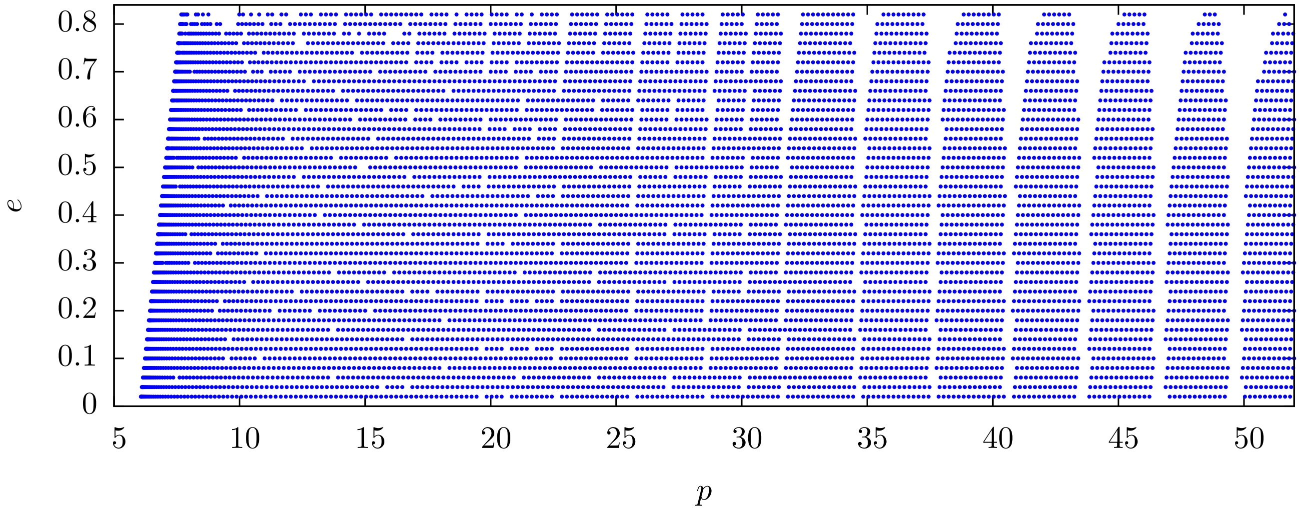

FIG. 3. Data used for interpolation of the oscillatory self-force. We computed data for 9602 unique orbits at a cost of 2308 CPU hours. The adiabatic data is computed over approximately the same domain, but with four times the density and no gaps due to orbital resonances. Explicitly, we computed adiabatic data for 43875 unique orbits at a cost of 2054 CPU hours. Most of the gaps in the dataset correspond to orbital resonances where small (non-zero) Fourier-mode frequencies are encountered (these modes are difficult for our Lorenz-gauge code to compute [52]).

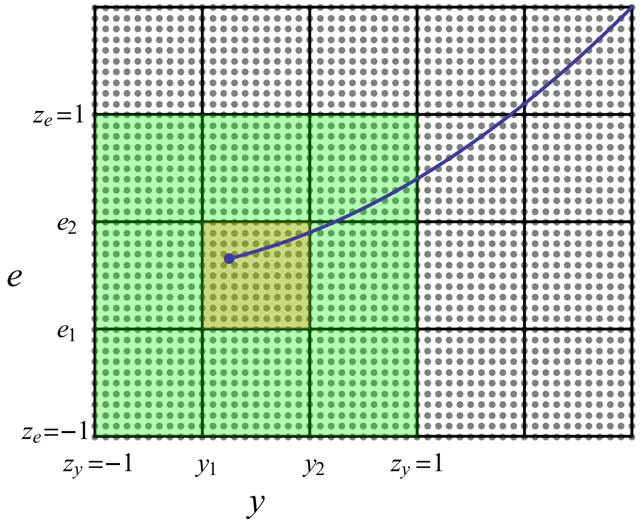

FIG. 4. The local discretization used for interpolation over the (e, y) parameter space (see Eq. (6.1) for the defintion of y). The blue line represents the inspiral trajectory with a point at the current position. The yellow zone is the inspiral's current sub-domain. The interpolation is performed with data (gray dots) from the yellow and green zones.

and $0 \leq e \leq 0.2$ by performing global fits to power series in p and e. Global fits are challenging to work as the fit has to incorporate the post-Newtonian-like behavior of the self-force in the weak field as well as the behaviour in the strong-field using a small set of parameters. As such the fidelity of the model is reduced. In this work we use a local fitting procedure. This results in a great deal more parameters that describe how the self-force varies over the parameter space, but in exchange the fidelity of our interpolation model is greatly improved. In fact, the accuracy of our model is within an order of magnitude of the underlying data.

Our local interpolation scheme begins by subdividing the domain into a grid of smaller rectangular zones. To obtain the self-force in a particular zone (with domain $e_1 \leq e < e_2$, $y_1 \leq y < y_2$) we interpolate using data from the nearest 9 zones (all the surrounding rectangles including the current one; see Fig. 4). We re-scale e and y into new variables z_e and z_y that equal -1 at the leading edge of the interpolation region and $+1$ at the trailing edge of the interpolation region. We then make a Chebyshev interpolation

$$z_e \equiv \frac{2e - e_2 - e_1}{3(e_2 - e_1)}, \qquad z_y \equiv \frac{2y - y_2 - y_1}{3(y_2 - y_1)}, \tag{6.4}$$

$$a_n^\alpha = \sum_{i=0}^{i_{\max}} \sum_{j=0}^{j_{\max}} \sigma_{nij}^\alpha T_i(z_e) T_j(z_y), \tag{6.5}$$

where $T_i(z)$ is the Chebyshev polynomial of the first kind. To ensure the correct units, σ_{nij}^t and σ_{nij}^r are implied to have overall factors of M^{-2} while σ_{nij}^φ is implied to have an overall factor of M^{-3}. We evaluate Eq. (6.5) for every data point in the interpolation region, which is a linear system for the unknown coefficients σ_{nij}^α. We require that the number of equations be greater than the number of unknowns, or equivalently that the number of data points is greater than $(i_{\max} + 1) \times (j_{\max} + 1)$. We use least-squares fitting to compute σ_{nij}^α. This fit is pre-computed for every sub-domain to facilitate rapid

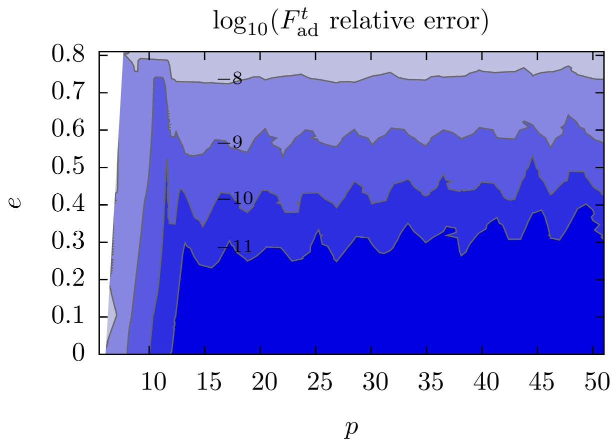

FIG. 5. Estimates of interpolation error in adiabatic part of self-force. We estimate the interpolation error of $F^t_{\rm ad}$ by computing orbits independent of those used for fitting interpolation coefficients and comparing with interpolated self-force values. The interpolation model recovers $F^t_{\rm ad}$ across parameter space with an error no worse than $\sim 10^{-8}$ (better for lower eccentricities and away from the separatrix). Similar results are observed for the other components of the self-force.

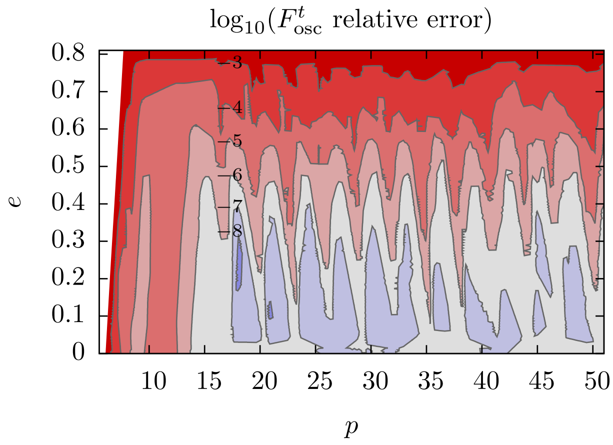

FIG. 6. Estimates of interpolation error in oscillatory part of self-force. We estimate the interpolation error of $F^t_{\rm osc}$ by computing orbits independent of those used for fitting interpolation coefficients and comparing with interpolated self-force values. The interpolation model recovers $F^t_{\rm osc}$ across parameter space with an error no worse than $\sim 10^{-3}$ (better for lower eccentricities and away from the separatrix). The larger error at high eccentricity is a limitation of the underlying data from the Lorenz-gauge code and motivates the hybrid scheme. Similar results are observed for the other components of the self-force.

numerical evaluation. Once the interpolation coefficients σ^α_{nij} are known for each sub-domain Eqs. (6.3) and (6.5) give the interpolated self-force.

For the adiabatic self-force interpolation we use 145 y-zones, 20 e-zones, and take $i_{\rm max} = j_{\rm max} = 12$. For the oscillatory (and non-hybrid) self-force interpolation we use 72 y-zones, 10 e-zones, and we take $i_{\rm max} = j_{\rm max} = 10$. To check the accuracy of the interpolation we compute the self-force for orbits not used in the fit for interpolation coefficients and compare with the interpolated result (see Figs. 5 and 6).

VII. INITIAL CONDITIONS WITH MATCHED FREQUENCIES

A number of works have argued that the gravitational waveforms from inspirals computed using only the adiabatic self-force will be sufficient for detection with space-based detectors [63, 95, 96]. The best way to assess this claim is by comparing inspirals computed with and without the oscillatory and conservative self-force corrections. The question then arises of how should one compare two such inspirals? In answering this question it is important to remember that an adiabatic inspiral and an inspiral computed using the full self-force live in two different spacetimes[4] so that a direct coordinate comparison (say by setting the initial $p, e, \chi_0, \varphi_p, t_p$ the same for both inspirals) is not ideal. A more appropriate comparison can be made by choosing the initial (gauge invariant) frequencies of the orbit to be the same. The utility of adiabatic self-force inspirals can then be assessed by comparing the accumulated azimuthal phase with that from an inspiral computed using the full self-force.

Before we consider how to match the initial inspiral frequencies in practice let us briefly discuss why simply matching the values of p and e for each inspiral is not optimal. The goal is to provide initial conditions for the approximate inspiral that minimises the phase difference with an inspiral computed using the full self-force. For clarity we'll consider the case for quasi-circular orbits where there is only one orbital frequency. For each inspiral we can expand the phase evolution in a Taylor series about $t_p = 0$ and write the difference between the two inspirals as:

$$\Delta\varphi_p(t_p) = (\varphi_0^{\rm apx} - \varphi_0^{\rm full}) + \left(\Omega_\varphi^{\rm apx} - \Omega_\varphi^{\rm full}\right) t_p + \mathcal{O}(t_p^2), \tag{7.1}$$

where an 'apx' superscript denotes a quantity associated with the inspiral that is computed using an approximation to the full self-force. Examples of such approximations are the adiabatic approximation, calculated by flux balance arguments, or the dissipative approximation, which excludes the conservative effects but retains the oscillatory dissipative self-force. The 'full' superscript denotes a quantity associated with an inspiral computed using the full self-force. Without loss of generality we can set $\varphi_0^{\rm apx} = \varphi_0^{\rm full}$ and then from Eq. (7.1) we see that equating the two initial orbital frequencies will remove

---

[4] for instance, by artificially turning off the conservative self-force, one is excluding the conservative part of the metric perturbation

the initial linear growth in the phase difference. With the frequencies matched the phase difference will still grow in time, but at the slower quadratic rate.

In order to match the initial frequencies for an eccentric inspiral we must find values of p_0 and e_0 for each inspiral such that

$$\Omega_\varphi^{\rm apx}(p_0^{\rm apx}, e_0^{\rm apx}) - \Omega_\varphi^{\rm full}(p_0^{\rm full}, e_0^{\rm full}) = 0 \tag{7.2}$$

$$\Omega_r^{\rm apx}(p_0^{\rm apx}, e_0^{\rm apx}) - \Omega_r^{\rm full}(p_0^{\rm full}, e_0^{\rm full}) = 0. \tag{7.3}$$

In general, setting $p_0^{\rm apx} = p_0^{\rm full}$ and $e_0^{\rm apx} = e_0^{\rm full}$ will not match the frequencies. Instead, we match the frequencies using the following procedure. We choose values for $p_0^{\rm full}$ and $e_0^{\rm full}$, calculate $\Omega_\varphi^{\rm full}$ and $\Omega_r^{\rm full}$, and then use a root finding algorithm to find the values of $p_0^{\rm apx}$ and $e_0^{\rm apx}$ that gives the same value for the initial frequencies for the approximate inspiral. It is interesting to note that the relation between the orbital frequencies and (p, e) is not one-to-one for orbits near the separatrix in the (p, e) parameter space [97]. Nonetheless, so long as the frequency matching is performed far from the separatrix, as is always the case in this work, there is no ambiguity in matching the frequencies.

Calculating the orbital frequencies including the self-force corrections is achieved by integrating the osculating orbit equations over one orbital period. Explicitly, we change the integration variable from χ to $v = \chi - \chi_0$ (using $dv/d\chi = 1 - d\chi_0/d\chi$) in Eqs. (4.10),(4.11),(4.16)-(4.18) and integrate the equations from $v = 0$ to $v = 2\pi$, using the relevant approximation to the self-force in Eqs. (4.16)-(4.18). The time elapsed and azimuthal phase accumulated between periastron passage we denote by T_r and $\Delta\varphi$. Equations (4.14) can then be used to compute the associated frequencies.

VIII. HIGHLY-ECCENTRIC INSPIRAL RESULTS

In this section we present our main results–a sample of inspirals computed using our hybrid geodesic self-force inspiral model. The physical results for extreme- and intermediate-mass-ratio inspirals are presented in Sec. VIII B. First, though, we quantify the performance of our hybrid self-force method.

A. Performance of the hybrid self-force method

Our hybrid scheme aims to produce a self-force that is sufficiently accurate to capture the leading and subleading contributions to the inspiral phase from the first-order-in-the-mass-ratio self-force. As discussed earlier, the raw self-force output from the Lorenz-gauge code does not meet this requirement for all eccentricities, and so we supplement those results with high-accuracy flux data from a RWZ code (see Sec. V B).

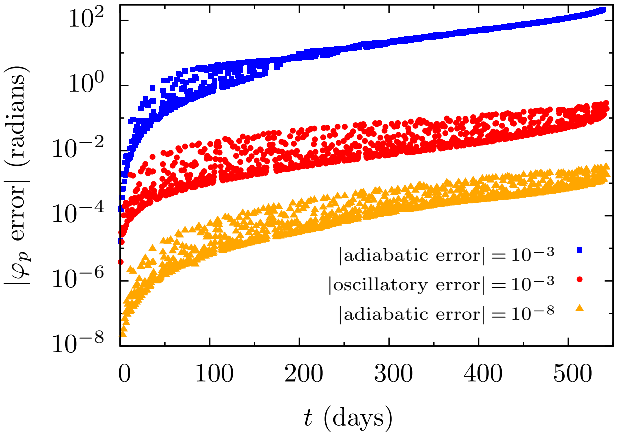

FIG. 7. Sensitivity of inspiral phase to error in the self-force. We test the sensitivity of the inspiral phase, φ_p, to errors in $F^\alpha_{\rm ad}$ and $F^\alpha_{\rm osc}$ by independently perturbing each part of the self-force with uniform errors of the indicated relative size, δ. At a relative size of δ, the expectation is that trial errors introduced in the adiabatic part of the self-force should have an effect that is a factor ϵ^{-1} larger than the effect of comparable errors injected in the oscillatory part of the self-force. The observed ratio is less dramatic but nevertheless indicates that computing the adiabatic part more accurately by orders of magnitude is crucial. The inspiral parameters were set to be $e_0 = 0.7$, $p_0 = 10$, $\chi_{00} = 0$, and $\epsilon = 10^{-5}$. The timescale is set by assuming $M = 10^6 M_\odot$.

To test whether our hybrid method allows the accumulated phase of an inspiral to be tracked to within ~ 0.1 radians, we perform several sensitivity tests. The sensitivity of the inspiral phase to a relative error δ in the oscillatory part of the self-force is tested by computing two inspirals, one where we introduce a uniform positive perturbation (trial error) $F^\alpha_{\rm osc} \to (1+\delta)F^\alpha_{\rm osc}$ and another where we introduce a uniform negative perturbation $F^\alpha_{\rm osc} \to (1-\delta)F^\alpha_{\rm osc}$. The absolute response in the orbital elements to these introduced errors is estimated by calculating the half-difference between the two perturbed inspirals. With the sensitivity to errors in the oscillatory part of the self-force tested, we then make an equivalent test on the adiabatic part, $F^\alpha_{\rm ad}$.

Figs. 5 and 6 showed previously that the adiabatic and oscillatory parts of the self-force in the hybrid scheme are accurate to at least 10^{-8} and 10^{-3}, respectively, and to much higher accuracy over most of orbital parameter space. The issue then is whether these error levels translate into requisite bounds on phase error. To determine this we ran the error sensitivity tests with error injections at these levels. In Fig. 7, we perturbed the adiabatic and oscillatory components of the self-force with relative errors of $\pm 10^{-8}$ (yellow) and $\pm 10^{-3}$ (red), respectively. We then tracked the relative drift in the cumulative azimuthal phase during the inspiral. For $\epsilon = 10^{-5}$ we find that a $\delta = 10^{-8}$ perturbation in $F^\alpha_{\rm ad}$ induces a $\sim 10^{-3}$ radian error in φ_p. For $F^\alpha_{\rm osc}$, a perturbation of $\delta = 10^{-3}$

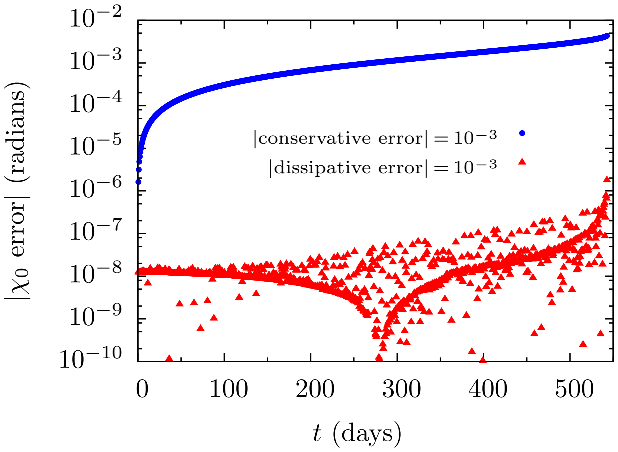

FIG. 8. Sensitivity in the evolution of χ_0 to error in the radial self-force. To test the propagation of errors into χ_0, we perturbed the force components in the χ_0 evolution equation while leaving the e and p evolution equations unaffected. Furthermore, we independently introduced errors into $F^r_{\rm cons}$ and $F^r_{\rm diss}$ in the χ_0 equation. At the worst case error level, the $F^r_{\rm diss}$ clearly has little influence on the evolution of χ_0. Since only the dissipative self-force is affected by hybridization, we see that the hybrid force is not essential in the evolution of χ_0. We also see that, at this same error level, the conservative self-force is accurate enough to hold errors in χ_0 to 0.01 radians or less. The inspiral parameters were $e_0 = 0.7$, $p_0 = 10$, $\chi_{00} = 0$, and $\epsilon = 10^{-5}$. The timescale is set by assuming $M = 10^6 M_\odot$.

causes an absolute error of ~ 0.1 radians in φ_p. We conclude that the numerical accuracy of the hybrid self-force model is sufficient to hold phase errors to less than 0.1 radians at the highest eccentricities $e \sim 0.7$. At lower eccentricities the inspiral phase error is smaller by orders of magnitude. Also indicated in the plot (blue) is the phase drift that would result for a $e = 0.7$ inspiral if only the Lorenz-gauge self-force had been used, demonstrating clearly the need to isolate the adiabatic part and compute it to higher accuracy (i.e., use the hybrid model).

As discussed in Sec. V B, within our scheme we create hybrid self-force values for F^t and F^φ but do not create a hybridized F^r. In principle $F^r_{\rm hyb}$ could be computed using $F^\alpha_{\rm hyb} u_\alpha = 0$ but such a construction involves dividing by u^r, which vanishes at the radial turning points. Instead we use the Lorenz-gauge (non-hybrid) F^r when computing the evolution of χ_0 (F^r is not directly required to evolve p and e as we write their evolution equations in terms of F^t and F^φ only). To ensure that using the non-hybrid result for F^r does not adversely affect our results, we made a sensitivity test in the evolution of χ_0. As Fig. 8 indicates, the dissipative part of F^r, which is the element that would be affected by hybridization, has little influence on the evolution of χ_0. Instead, as the figure shows, it is the conservative part of F^r that dominates the evolution of χ_0, and our scheme is accurate enough to hold errors in χ_0 to 0.01 radians.

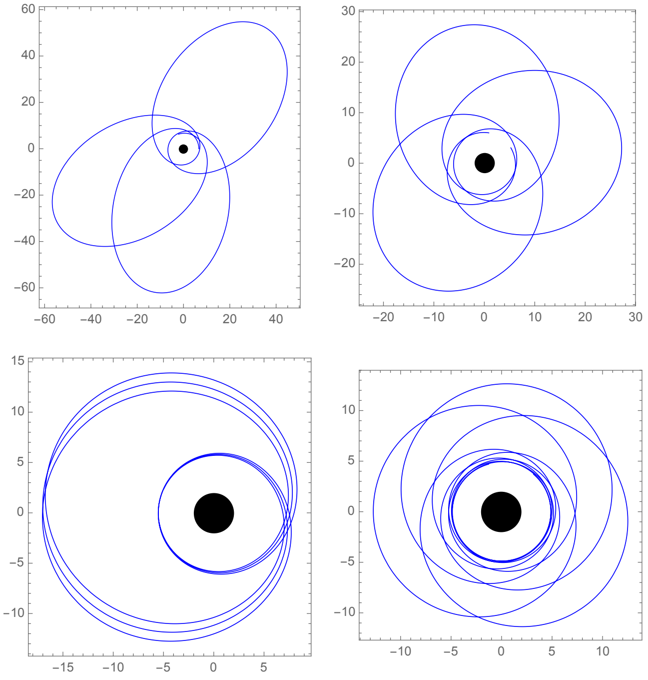

FIG. 9. Sample snapshots of an inspiral with $M = 10^6 M_\odot$ and $\epsilon = 10^{-5}$. The inspiral is plotted in Boyer-Lindquist coordinates with $x = (r_p/M)\cos(\varphi_p), y = (r_p/M)\sin(\varphi_p)$. Each snapshot shows three periastron passages of the (counter-clockwise moving) inspiral and the central black hole is drawn to scale. The initial configuration is ~ 2115.5 days from plunge and is shown in the top left panel. The initial parameters are $p = 15, e = 0.81$ (this corresponds to $p = 0.1183$ AU). The other panels show 500 days until plunge (top right), 100 days to plunge (bottom left) and 1 day until plunge (bottom right). The inspiral depicted here corresponds to the second-from-the-left black curve in the Fig. 10. The orbital configuration in the bottom-left panel is near a 1:2 r-φ resonance which, in principle, could provide a substantial kick to the linear-momentum of the binary [98]. We have not attempted to explore this effect in this work.

B. EMRI and IMRI results

Using the interpolated hybrid self-force we computed a set of trajectories of extreme-mass-ratio-inspirals using the osculating element equations. In Fig. 9 we show snapshots of a sample high-eccentricity inspiral, computed with $M = 10^6 M_\odot$, $\epsilon = 10^{-5}$ and $(p_0, e_0) = (12, 0.81)$. For a sense of scale, at the initial configuration the inspiral's apastron is at ~ 0.623 AU and its periastron is at ~ 0.0654 AU; the entire inspiral occurs in the strong-field regime. In this example the EMRI takes 2115.45 days to evolve to plunge, during which it undergoes ~ 50132 periastron passages. Computing this particular inspiral took a few minutes on a standard 3GHz laptop.

Over an inspiral the values of p and e generally decrease (with the possible exception of a small increase in eccentricity close to plunge [93]). This behaviour is best seen in a (p, e) plot of the inspirals such as the one we

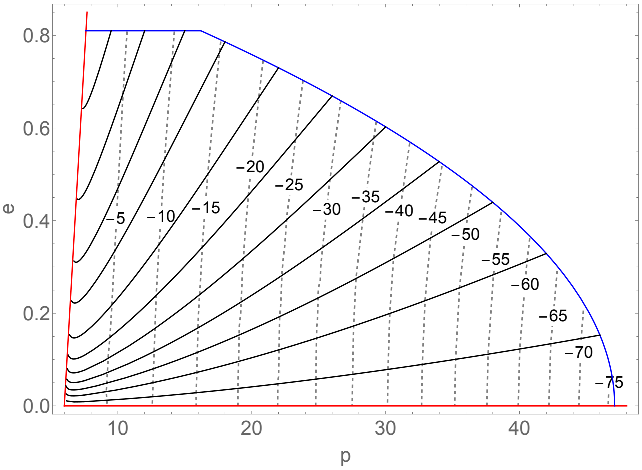

FIG. 10. Sample inspirals for $\mu/M = 10^{-5}$ and $M = 10^6 M_\odot$. Solid black curves show the evolution of (p, e) from entering the LISA-like passband (marked with the blue curve). We truncate this curve to a constant in e for $p \lesssim 16$ as it is predicted that the initial eccentricity of EMRIs will not be above ~ 0.81 [49]. Generally, as each inspiral progresses, both p and e decrease (with the exception of an increase in e near the separatrix [93]). The dashed lines are contours that mark the number of radians χ_0 will evolve from a given point until plunge (this number is negative as the conservative self-force, and hence evolution of χ_0, acts against the usual periastron advance [61]).

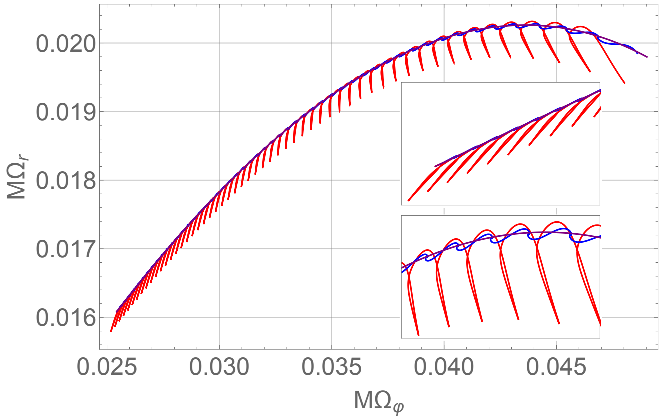

FIG. 11. Sample IMRI evolution. The evolution of the orbital frequencies for inspirals computed using the full self-force F^α (red curve), the dissipative self-force $F^\alpha_{\rm diss}$ (blue curve), and the adiabatic self-force $F^\alpha_{\rm ad}$ (non-oscillatory, purple curve). The mass ratio is $\epsilon = 5 \times 10^{-3}$. The full self-force evolution is started with $(p, e) = (10, 0.4)$ and the initial frequencies of the other inspirals are matched using the procedure outlined in Sec. VII. The upper inset shows the initial period of the evolutions where the different inspirals are in phase. The lower inset shows the inspirals close to plunge, where now the full and dissipative inspirals are starting to dephase. At plunge the total discrepancy of the accumulated phase between the full and dissipative only inspirals is ~ 2 radians.

show in Fig. 10. In this figure we show the tracks in p, e-space of a number of inspirals from the point when they enter the observable band of a LISA-like spacecraft until plunge. In addition we show, overlaid as a contour plot, the evolution of χ_0. As χ_0 is predominantly affected by the conservative self-force, we can use χ_0 to gauge the influence of the conservative self-force on an inspiral's phase. We see that the conservative self-force subtracts somewhere between 10 and 70 radians of phase for an inspiral that starts with $p > 14$. Note that although the tracks in Fig. 10 look very smooth, each track has many thousands of oscillations on the orbital timescale that are too small to appear on the plot.

The time to compute the tracks shown in Fig. 10 varies greatly, with the shortest being a few minutes and the longest being tens of hours on a standard 3GHz laptop. The reason for this large variation in computation time is that the self-force for orbits with a large value of p is much smaller (e.g., for circular orbits F^t scales as r_0^{-5} for large r_0 [27]). Consequently, inspirals evolve much more slowly in this regime. For example, the bottom most track in Fig. 10 starts with parameters $(p_0, e_0) = (46, 0.152822)$ and goes through over 6×10^6 periastron passages before plunge. In contrast, the left-most track only goes through $\sim 10^3$ periastron passages before plunge. The latter takes minutes to compute whereas the former takes many hours.

In addition to computing inspirals for EMRIs we can also consider results for IMRIs. For our evolution scheme to be valid the inspiral must evolve adiabatically, which will not be the case when ϵ is large and the particle is in the strong-field. Ref. [93] quantified the allowed range of mass-ratios and found that so long as $\epsilon \ll (p - 6 - 2e)^2$ the inspiral will evolve adiabatically[5]. We thus see that even quite close to the separatrix our inspirals should be valid. In addition, recent work has shown that the domain of validity of the conservative sector of perturbation theory likely includes IMRIs [38]. For this reason we include an example IMRI inspiral. As IMRIs evolve much faster than EMRIs, this gives us an opportunity to showcase the effects of the self-force on the inspiral on the orbital timescale. We also take the opportunity to compare our inspiral computed using the full self-force with that computed using an adiabatic approximation and a dissipative-only approximation (matching the initial frequencies as outlined in Sec. VII).

Our main result on IMRIs is presented in Fig. 11 where we show the evolution of the orbital frequencies for inspirals computed with $\epsilon = 5 \times 10^{-3}$ and initial conditions $p_0 = 10$, $e_0 = 0.4$. When the initial frequencies are matched, the full self-force inspiral, dissipative-only inspiral, and adiabatic inspiral initially evolve together. The conservative self-force induces large oscillations in the orbital frequencies on the orbital timescale, whereas the dissipative only inspiral has smaller oscillations and

---

[5] Near the ISCO this condition is modified to $\epsilon \ll (p - 6)^{5/2}$

the adiabatic inspiral exhibits no oscillations. Even in this short inspiral, which lasts just 8 minutes, excluding the conservative self-force causes the inspiral to dephase by 2 radians.

IX. CONCLUDING REMARKS

In this paper we have computed high-eccentricity inspirals of a stellar-mass compact object into a massive Schwarzschild black hole while including all first-order-in-the-mass-ratio effects. A key feature of this work over previous efforts is that we are able to model inspirals with an initially high eccentricity as they enter the detection band of a LISA-like spacecraft (previous work concentrated on the low-eccentricity case [54, 55]). This is important because it is expected that most observed EMRIs will initially be highly eccentric [49].

In computing inspirals we make use of a new code to compute the local Lorenz-gauge self-force acting on the particle [52]. Although this code is a marked improvement on previous codes [28, 30] in terms of speed and accuracy, the raw output of the code is not sufficiently accurate across the whole parameter space of inspirals to allow for the computation of inspirals with a phase error of less than 0.1 radians. To overcome this we note that the leading-order phase evolution is driven by the orbit-averaged fluxes radiated from the particle. This inspires a hybrid scheme of combining the Lorenz-gauge results with fluxes calculated from a highly-accurate RWZ code. The hybrid self-force is then pre-computed to densely cover a wide region of orbital parameter space. We are then able to implement a relatively local interpolation scheme for the self-force to rapidly compute extreme and intermediate-mass-ratio inspirals. Typically an inspiral starting in the strong field will take a few minutes on a standard 3GHz laptop to evolve to plunge. Our main results are presented in Sec. VIII B.

Looking to the future, there are a number of open questions remaining. First, in order to complete the inspiral model, accurate to less than order unity in the phase evolution, it will be necessary to include second-order-in-the-mass-ratio effects [66] (see Table I). Currently there are no calculations of the second-order self-force, but the necessary formalism has been laid [75] and computational techniques are emerging [79, 80]. Once the second-order orbit averaged dissipative self-force can be computed, the results are easily added to our self-force interpolation scheme and inspiral model.

It will also be important to quantify the effects of the "geodesic self-force approximation." The true self-force is a functional of the entire past history of the particle's motion but in our work we take the self-force at each instance to be that of a particle whose past history is motion along the tangent geodesic to the inspiralling worldline. This approximation introduces a small error which is important to quantify. Initial investigations made by comparing a self-consistent evolution with a geodesic self-force evolution in the scalar case suggest this error is very small (with the phase error smaller than the error-bars from either evolution [57–59]). Once self-consistent evolutions can be made in the gravitational case the results of our work here can be used for comparison to quantify the error from the geodesic self-force approximation.

In our work we concentrated on inspirals into a Schwarzschild black hole but it is expected that astrophysical black holes will generally be rotating. Thus it is important to extend inspiral models to motion around a Kerr black hole. There has been much progress recently on computing self-forces in Kerr spacetime [32, 48, 99, 100] and these results can be used to compute inspirals in much the same way as we have done here. Orbits in Kerr spacetime are generally computed in a radiation gauge. Thus, even in Schwarzschild spacetime, it would be interesting to compare an evolution computed using a radiation gauge self-force with our evolution computed using a Lorenz-gauge self-force. Whilst the coordinate descriptions of the two evolutions might differ, the phase evolution should be the same.

Finally, we note that although we can rapidly compute inspirals in a matter of minutes, this is probably still not quick enough for use in practical matched filtering searches. A similar problem is encountered when evaluating the time-domain EOB models for use in gravitational-wave searches with LIGO data. One successful technique that has been applied in that case is the use of Reduced Order Modelling [94] that allows for interpolation and rapid evaluation of the EOB waveforms. No doubt a similar approach would be beneficial for more extreme mass ratios as well.

ACKNOWLEDGMENTS

We thank Chad Galley, Scott Field, Barry Wardell and Seth Hopper for helpful discussions. We also thank Sarp Akcay for a careful reading and comments on a draft of this paper. This work was supported in part by NSF grant PHY-1506182. N.W. gratefully acknowledges support from a Marie Curie International Outgoing Fellowship (PIOF-GA-2012-627781). T.O. gratefully acknowledges support from the North Carolina Space Grant's Graduate Research Assistantship Program and a Dissertation Completion Fellowship from the UNC Graduate School. C.R.E. acknowledges support from the Bahnson Fund at the University of North Carolina-Chapel Hill.

---

[1] "LIGO home page," http://www.ligo.caltech.edu/.

[2] "VIRGO home page," http://www.ego-gw.it/.

[3] "KAGRA home page," `http://gwcenter.icrr.u-tokyo.ac.jp/en/`.

[4] P. A. Seoane *et al.* (eLISA), (2013), arXiv:1305.5720.

[5] L. Blanchet, Living Reviews in Relativity **17**, 2 (2014), arXiv:1310.1528.

[6] T. W. Baumgarte and S. L. Shapiro, *Numerical Relativity: Solving Einstein's Equations on the Computer* (Cambridge University Press, 2010).

[7] L. Lehner and F. Pretorius, Annu. Rev. Astron. Astrophys. **52**, 661 (2014), arXiv:1405.4840.

[8] L. Barack, Class. Quant. Grav. **26**, 213001 (2009), arXiv:0908.1664.

[9] E. Poisson, A. Pound, and I. Vega, Living Rev. Rel. **14**, 7 (2011), arXiv:gr-qc/1102.0529.

[10] J. Thornburg, GW Notes, Vol. 5, p. 3-53 **5**, 3 (2011), arXiv:1102.2857.

[11] A. Buonanno and T. Damour, Phys. Rev. D **59**, 084006 (1999), gr-qc/9811091.

[12] A. Buonanno, Y. Pan, H. P. Pfeiffer, M. A. Scheel, L. T. Buchman, and L. E. Kidder, Phys. Rev. D **79**, 124028 (2009), arXiv:0902.0790.

[13] T. Damour, Phys. Rev. D **81**, 024017 (2010), arXiv:0910.5533.

[14] S. J. Vigeland and S. A. Hughes, Phys. Rev. D **81**, 024030 (2010), arXiv:0911.1756.

[15] L. Barack and C. Cutler, Phys. Rev. D **75**, 042003 (2007), arXiv:gr-qc/0612029.

[16] D. A. Brown, J. Brink, H. Fang, J. R. Gair, C. Li, G. Lovelace, I. Mandel, and K. S. Thorne, Physical Review Letters **99**, 201102 (2007), gr-qc/0612060.

[17] J. R. Gair, M. Vallisneri, S. L. Larson, and J. G. Baker, Living Rev. Rel. **16**, 7 (2013), arXiv:1212.5575.

[18] E. Barausse, V. Cardoso, and P. Pani, Phys. Rev. **D89**, 104059 (2014), arXiv:1404.7149.

[19] P. Amaro-Seoane, J. R. Gair, M. Freitag, M. C. Miller, I. Mandel, C. J. Cutler, and S. Babak, Class. Quant. Grav. **24**, R113 (2007), arXiv:astro-ph/0703495.

[20] M. C. Miller and E. J. M. Colbert, International Journal of Modern Physics D **13**, 1 (2004).

[21] Y. Mino, M. Sasaki, and T. Tanaka, Phys. Rev. D **55**, 3457 (1997).

[22] T. C. Quinn and R. M. Wald, Phys. Rev. D **56**, 3381 (1997).

[23] L. Barack and A. Ori, Phys. Rev. D **61**, 061502 (2000), arXiv:gr-qc/9912010.

[24] S. L. Detweiler and B. F. Whiting, Phys. Rev. D **67**, 024025 (2003), arXiv:gr-qc/0202086.

[25] S. E. Gralla and R. M. Wald, Class.Quant.Grav. **25**, 205009 (2008), arXiv:0806.3293.

[26] A. Pound, Phys. Rev. D **81**, 024023 (2010), arXiv:0907.5197.

[27] L. Barack and N. Sago, Phys. Rev. D **75**, 064021 (2007), arXiv:gr-qc/0701069.

[28] L. Barack and N. Sago, Phys. Rev. D **81**, 084021 (2010), arXiv:1002.2386.

[29] S. Akcay, Phys. Rev. D **83**, 124026 (2011).

[30] S. Akcay, N. Warburton, and L. Barack, Phys. Rev. D **88**, 104009 (2013), arXiv:1308.5223.

[31] S. R. Dolan and L. Barack, Phys. Rev. D **87**, 084066 (2013), arXiv:1211.4586.

[32] C. Merlin and A. G. Shah, Phys. Rev. D **91**, 024005 (2015), arXiv:1410.2998.

[33] S. Detweiler, Phys. Rev. D **77**, 124026 (2008), arXiv:0804.3529.

[34] S. R. Dolan, N. Warburton, A. I. Harte, A. Le Tiec, B. Wardell, and L. Barack, Phys. Rev. D **89**, 064011 (2014), arXiv:1312.0775.

[35] S. R. Dolan, P. Nolan, A. C. Ottewill, N. Warburton, and B. Wardell, Phys. Rev. D **91**, 023009 (2015), arXiv:1406.4890.

[36] P. Nolan, C. Kavanagh, S. R. Dolan, A. C. Ottewill, N. Warburton, and B. Wardell, (2015), arXiv:1505.04447.

[37] L. Blanchet, S. Detweiler, A. Le Tiec, and B. F. Whiting, Phys. Rev. D **81**, 064004 (2010), arXiv:0910.0207.

[38] A. Le Tiec, A. H. Mroué, L. Barack, A. Buonanno, H. P. Pfeiffer, N. Sago, and A. Taracchini, Physical Review Letters **107**, 141101 (2011), arXiv:1106.3278.

[39] S. Akcay, L. Barack, T. Damour, and N. Sago, Phys. Rev. D **86**, 104041 (2012), arXiv:1209.0964.

[40] D. Bini and T. Damour, Phys. Rev. D **89**, 064063 (2014), arXiv:1312.2503.

[41] D. Bini and T. Damour, Phys. Rev. D **90**, 024039 (2014), arXiv:1404.2747.

[42] D. Bini and T. Damour, Phys. Rev. D **90**, 124037 (2014), arXiv:1409.6933.

[43] S. Isoyama, L. Barack, S. R. Dolan, A. Le Tiec, H. Nakano, A. G. Shah, T. Tanaka, and N. Warburton, Phys. Rev. Lett. **113**, 161101 (2014), arXiv:1404.6133.

[44] A. G. Shah, J. L. Friedman, and B. F. Whiting, Phys. Rev. D **89**, 064042 (2014), arXiv:1312.1952.

[45] C. Kavanagh, A. C. Ottewill, and B. Wardell, Phys. Rev. D **92**, 084025 (2015), arXiv:1503.02334.

[46] A. G. Shah and A. Pound, Phys. Rev. D **91**, 124022 (2015), arXiv:1503.02414.

[47] S. Akcay, A. Le Tiec, L. Barack, N. Sago, and N. Warburton, Phys. Rev. D **91**, 124014 (2015), arXiv:1503.01374.

[48] M. van de Meent and A. G. Shah, Phys. Rev. D **92**, 064025 (2015), arXiv:1506.04755.

[49] C. Hopman and T. Alexander, Astrophysical Journal **629**, 362 (2005), arXiv:astro-ph/0503672.

[50] S. Drasco and S. A. Hughes, Phys. Rev. D **73**, 024027 (2006), gr-qc/0509101.

[51] R. Fujita, W. Hikida, and H. Tagoshi, Prog. Theor. Phys. **121**, 843 (2009), arXiv:0904.3810.

[52] T. Osburn, E. Forseth, C. R. Evans, and S. Hopper, Phys. Rev. D **90**, 104031 (2014), arXiv:1409.4419.

[53] N. Warburton and L. Barack, Phys. Rev. D **83**, 124038 (2011), arXiv:1103.0287.

[54] N. Warburton, S. Akcay, L. Barack, J. R. Gair, and N. Sago, Phys. Rev. D **85**, 061501 (2012), arXiv:1111.6908.

[55] K. A. Lackeos and L. M. Burko, Phys. Rev. D **86**, 084055 (2012), arXiv:1206.1452.

[56] A. Pound, *Proceedings, 524th WE-Heraeus-Seminar: Equations of Motion in Relativistic Gravity (EOM 2013)*, Fund. Theor. Phys. **179**, 399 (2015), arXiv:1506.06245.

[57] N. Warburton (2013) , Talk presented at the 16th Capra meeting held at University College Dublin, `http://maths.ucd.ie/capra16/schedule/`.

[58] N. Warburton (2014) , Talk presented at the 17th Capra meeting held at Caltech, `http://www.tapir.caltech.edu/~capra17/Schedule.shtml`.

[59] P. Diener (2015) , Talk presented at the 18th Capra meeting held at Kyoto University, `http://www2.yukawa.kyoto-u.ac.jp/~capra18/`.

[60] C. Misner, K. Thorne, and J. Wheeler, *Gravitation* (Freeman, San Francisco, CA, U.S.A., 1973).
[61] L. Barack and N. Sago, Phys. Rev. D **83**, 084023 (2011), arXiv:1101.3331.
[62] A. Pound and E. Poisson, Phys. Rev. D **77**, 044013 (2008), arXiv:0708.3033.
[63] S. A. Hughes, S. Drasco, E. E. Flanagan, and J. Franklin, Phys. Rev. Lett. **94**, 221101 (2005), arXiv:gr-qc/0504015.
[64] S. Drasco, E. E. Flanagan, and S. A. Hughes, Classical and Quantum Gravity **22**, S801 (2005).
[65] T. Tanaka, Progress of Theoretical Physics Supplement **163**, 120 (2006), gr-qc/0508114.
[66] T. Hinderer and E. E. Flanagan, Phys. Rev. D **78**, 064028 (2008), arXiv:0805.3337.
[67] Y. Mino, Phys. Rev. D **67**, 084027 (2003), arXiv:gr-qc/0302075.
[68] N. Sago, T. Tanaka, W. Hikida, and H. Nakano, Prog. Theor. Phys. **114**, 509 (2005), arXiv:gr-qc/0506092.
[69] N. Sago, T. Tanaka, W. Hikida, K. Ganz, and H. Nakano, Prog. Theor. Phys. **115**, 873 (2006), arXiv:gr-qc/0511151.
[70] E. E. Flanagan and T. Hinderer, Phys. Rev. Lett. **109**, 071102 (2012), arXiv:1009.4923.
[71] U. Ruangsri and S. A. Hughes, Phys. Rev. D **89**, 084036 (2014), arXiv:1307.6483.
[72] J. Brink, M. Geyer, and T. Hinderer, Phys. Rev. Lett. **114**, 081102 (2015), arXiv:1304.0330.
[73] M. van de Meent, Phys. Rev. D **89**, 084033 (2014), arXiv:1311.4457.
[74] J. Brink, M. Geyer, and T. Hinderer, Phys. Rev. D **91**, 083001 (2015), arXiv:1501.07728.
[75] A. Pound, Phys. Rev. Lett. **109**, 051101 (2012), arXiv:1201.5089.
[76] S. E. Gralla, Phys. Rev. D **85**, 124011 (2012), arXiv:1203.3189.
[77] S. Detweiler, Phys. Rev. D **85**, 044048 (2012), arXiv:1107.2098.
[78] A. Pound and J. Miller, Phys. Rev. D **89**, 104020 (2014), arXiv:1403.1843.
[79] N. Warburton and B. Wardell, Phys. Rev. D **89**, 044046 (2014), arXiv:1311.3104.
[80] B. Wardell and N. Warburton, Phys. Rev. D **92**, 084019 (2015), arXiv:1505.07841.
[81] P. Diener, I. Vega, B. Wardell, and S. Detweiler, Physical Review Letters **108**, 191102 (2012), arXiv:1112.4821.
[82] P. Diener (Private communication, 2015).
[83] K. G. Arun, L. Blanchet, B. R. Iyer, and M. S. S. Qusailah, Phys. Rev. D **77**, 064034 (2008), arXiv:0711.0250.
[84] L. M. Burko and G. Khanna, Phys. Rev. D **88**, 024002 (2013), arXiv:1304.5296.
[85] S. Hopper and C. R. Evans, Phys. Rev. D **82**, 084010 (2010), arXiv:1006.4907.
[86] S. Hopper, E. Forseth, T. Osburn, and C. R. Evans, Phys. Rev. D **92**, 044048 (2015), arXiv:1506.04742.
[87] J. R. Gair, É. É. Flanagan, S. Drasco, T. Hinderer, and S. Babak, Phys. Rev. D **83**, 044037 (2011), arXiv:1012.5111.
[88] C. Darwin, Proc. R. Soc. Lond. A **249**, 180 (1959).
[89] L. Barack, A. Ori, and N. Sago, Phys. Rev. D **78**, 084021 (2008), arXiv:0808.2315.
[90] A. Heffernan, A. Ottewill, and B. Wardell, Phys. Rev. D **86**, 104023 (2012), arXiv:1204.0794.
[91] W. H. Press, S. A. Teukolsky, W. T. Vetterling, and B. P. Flannery, *Numerical Recipes in C: The Art of Scientific Computing*, 2nd ed. (Cambridge University Press, Cambridge, UK, 1993).
[92] R. Fujita and W. Hikida, Classical and Quantum Gravity **26**, 135002 (2009), arXiv:0906.1420.
[93] C. Cutler, D. Kennefick, and E. Poisson, Phys. Rev. D **50**, 3816 (1994).
[94] S. E. Field, C. R. Galley, J. S. Hesthaven, J. Kaye, and M. Tiglio, Phys. Rev. X **4**, 031006 (2014), arXiv:1308.3565.
[95] J. R. Gair, L. Barack, T. Creighton, C. Cutler, S. L. Larson, E. S. Phinney, and M. Vallisneri, *8th Gravitational Wave Data Analysis Workshop (GWDAW 2003) Milwaukee, Wisconsin, December 17-20, 2003*, Class. Quant. Grav. **21**, S1595 (2004), arXiv:gr-qc/0405137.
[96] E. A. Huerta and J. R. Gair, Phys. Rev. D **79**, 084021 (2009), [Erratum: Phys. Rev. D 84, 049903 (2011)], arXiv:0812.4208.
[97] N. Warburton, L. Barack, and N. Sago, Phys. Rev. D **87**, 084012 (2013), arXiv:1301.3918.
[98] M. van de Meent, Phys. Rev. D **90**, 044027 (2014), arXiv:1406.2594.
[99] T. S. Keidl, A. G. Shah, J. L. Friedman, D.-H. Kim, and L. R. Price, Phys. Rev. D **82**, 124012 (2010), arXiv:1004.2276.
[100] A. Pound, C. Merlin, and L. Barack, Phys. Rev. D **89**, 024009 (2014), arXiv:1310.1513.